CNP blocks mitochondrial depolarization and inhibits SARS-CoV-2 replication *in vitro* and *in vivo*

James Logue[1,2], Victoria M. Melville[1,2], Jeremy Ardanuy[1,2], Matthew B. Frieman[1,2,*]

[1]The Department of Microbiology and Immunology, The University of Maryland School of Medicine, Baltimore,Maryland, USA.

[2]Center for Pathogen Research, The University of Maryland School of Medicine, Baltimore,Maryland, USA.

[*]Correspondence: M.B.F (mfrieman@som.umaryland.edu)

Abstract

The COVID-19 pandemic has claimed over 6.5 million lives worldwide and continues to have lasting impacts on the world's healthcare and economic systems. Several approved and emergency authorized therapeutics that inhibit early stages of the virus replication cycle have been developed however, effective late-stage therapeutical targets have yet to be identified. To that end, our lab identified that 2',3' cyclic-nucleotide 3'-phosphodiesterase (CNP) inhibits SARS-CoV-2 virion assembly. We show that CNP inhibits the generation of new SARS-CoV-2 virions, reducing intracellular titers without inhibiting viral structural protein translation. Additionally, we show that targeting of CNP to mitochondria is necessary for inhibition, blocking mitochondrial depolarization and implicating CNP's proposed role as an inhibitor of the mitochondrial permeabilization transition pore (mPTP) as the mechanism of virion assembly inhibition. We also demonstrate that an adenovirus expressing virus expressing both human ACE2 and CNP inhibits SARS-CoV-2 titers to undetectable levels in lungs of mice. Collectively, this work shows the potential of CNP to be a new SARS-CoV-2 antiviral target.

Author Summary

Upon entry into a cell, viruses manipulate the cellular environment for the benefit of their replication. We have found that upon infection, SARS-CoV-2 induces the mitochondria to release reactive oxygen species (ROS) into the cytoplasm which benefits the replication of the virus. We identified a phosphodiesterase, called CNP, that blocks this release via inhibition of an inducible pore called the mitochondrial permeability transition pore or mPTP. We also found that a drug targeting this pore inhibits SARS-CoV-2 replication. We test the function of CNP in vivo and find that if we overexpress CNP in mouse lungs, we inhibit SARS-CoV-2 replication. Together this demonstrates a key function of the mitochondria on SARS-CoV-2 replication and that antithetically ROS release enhances viral replication. We propose this is common across coronaviruses and potentially other viruses identifying a novel target for future therapies.

Introduction

Severe acute respiratory syndrome coronavirus 2 (SARS-CoV-2) is the etiologic agent of coronavirus disease 2019 (COVID-19), first reported in Wuhan City, Hubei Provence, China in December 2019 [1-3]. Since then, SARS-CoV-2 infections have expanded to a worldwide pandemic, with over 675 million reported cases and over 6.8 million reported deaths at the time of writing [4, 5]. In the absence of broad-spectrum, small molecule antiviral treatments, much of the early COVID-19 therapeutic research focused on the potential repurposing of compounds already approved by the United States Food and Drug Administration (FDA) for other diseases [6-8]. Though an overwhelming majority of compounds did not prove effective, a small number were tested in clinical trials, with only the nucleoside analogues Remdesivir and Molnupiravir receiving FDA Emergency Use Authorization or full approval for the treatment of early COVID-19 by the time of writing [9, 10]. In addition to repurposed compounds, SARS-CoV-2-specific therapies have been authorized or approved by the FDA, including the oral protease inhibitor Paxlovid and several monoclonal antibody treatments [11-14].

50 SARS-CoV-2 infection begins with binding of the surface protein Spike (S) to the cellular
51 receptor, angiotensin converting enzyme II (ACE2), following which S can be cleaved on the cell surface
52 by Transmembrane protease serine 2 (TMPRSS2) or by Cathepsins B or L in endosomes to facilitate
53 membrane fusion and viral genome release into the cytosol [15-21]. Nonstructural proteins are then
54 immediately translated to a polyprotein to be liberated into individual proteins by viral mediated
55 proteolysis, leading to the formation of replication organelles (DMVs) [22-25]. RNA replication then
56 occurs in these organelles, resulting in the generation of new viral genomes and the production of viral
57 subgenomic RNA (sgRNA), the coronavirus equivalent of mRNA, that are translated into structural and
58 accessory proteins [22, 26]. Assembly of new SARS-CoV-2 virions occurs at the ER-Golgi Intermediate
59 Compartment (ERGIC) followed by virus exit by a still undefined exocytotic method [27-29].
60 Interestingly, all therapeutics currently authorized or approved by the FDA target early stages of
61 the SARS-CoV-2 life cycle (e.g., entry, RNA replication). However, later stages of the SARS-CoV-2 life
62 cycle are relatively not well understood and, consequently, late-stage inhibitors that could prove more
63 effective or work synergistically with early-stage inhibitors are lacking. We previously identified 2', 3'-
64 cyclic nucleotide 3'-phosphodiesterase (CNP) as a late-lifecycle-stage SARS-CoV-2 inhibitor in an
65 overexpression screen of 399 interferon stimulated genes (ISGs) [30]. CNP is a lipid-bound protein that is
66 expressed throughout the body, including pulmonary tissues, but expressed at very high levels in myelin
67 [31-33]. Though early biochemical studies identified CNP by its ability to hydrolyze 2',3'-cyclic
68 nucleotides, as the name suggests, an exact function and a potential cellular substrate have yet to be
69 demonstrated *in vitro* or *in vivo* [34]. However, a growing pool of evidence has begun to establish
70 potential functions for the mitochondria-targeted isoform of CNP (CNP2), which has been shown to
71 inhibit opening of the mitochondrial permeabilization transition pore (mPTP), a process that leads to
72 mitochondrial depolarization in response to mitochondrial Ca^{2+} overload, cellular oxidative stress, or
73 potentially SARS-CoV-2 infection [35-39]. In our previous work, we showed CNP overexpression
74 inhibited SARS-CoV-2 replication in all the cell lines tested, including primary human tracheobronchial
75 epithelial cells, and further showed the inhibition to occur at a replication lifecycle stage post-genome

76 replication [30]. However, the exact lifecycle stage affected and the mechanism of action has yet to be
77 identified.

78 In this study, we confirm that overexpression of CNP *in vitro* has no effect on SARS-CoV-2
79 genome replication and further show CNP affects neither subgenomic RNA generation nor structural
80 protein translation. However, CNP overexpression reduced SARS-CoV-2 N localization to sites of virion
81 assembly (ERGIC) and reduced intracellular SARS-CoV-2 titers, providing strong evidence that virion
82 assembly is inhibited. Additionally, we show that CNP inhibition of SARS-CoV-2 required mitochondrial
83 targeting of CNP, which reduced SARS-CoV-2-induced mPTP opening and mitochondrial reactive
84 oxygen species (ROS) release. Indeed, replacing reactive oxygen species in CNP stably-expressing cells
85 through peroxide treatment resulted in a rescue of virus titer. Finally, we show that CNP overexpression
86 in Balb/c laboratory mouse lungs protected mice from SARS-CoV-2 infection, reducing lung virus titers
87 by over 1,000-fold. This work highlights the importance of cytosolic ROS for SARS-CoV-2 virion
88 assembly and identifies CNP as a potential therapeutic target for COVID-19.
89

90 ## Results

91 **CNP inhibits SARS-CoV-2 virion assembly.**

92 Previous data from our lab shows that CNP overexpression inhibits a SARS-CoV-2 lifecycle
93 stage post-genome replication [30]. To further elucidate the stages affected, HEK293T/hACE2 cells
94 stably expressing HA-tagged CNP or HA-tagged GFP were generated by lentivirus transduction (S1 Fig).
95 Cells were then infected with SARS-CoV-2/WA1 for a 45-minute absorption period followed by washing
96 with cell culture media to remove any remaining unbound virus. Various assays were then used to assess
97 the effects of CNP overexpression on multiple SARS-CoV-2 lifecycle stages. At 6-hours post-infection
98 (hpi), we confirmed that gRNA levels are not significantly different between CNP stable cells and GFP
99 stable cells (Fig 1A) and, further show that sgRNA levels are not altered by CNP (Fig 1B). At 12hpi,
100 western blots for SARS-CoV-2 structural proteins S and N were also not qualitatively different between

101 CNP and GFP stable cells, suggesting no effect on structural protein translation (Fig 1C). However, at
102 18hpi, SARS-CoV-2 titers were significantly lower when assessed for both intracellular titer (Fig 1D) and
103 extracellular titer (Fig 1E), suggesting the assembly of new SARS-CoV-2 virions is affected by CNP. As
104 SARS-CoV-2 virion assembly takes place at the ERGIC, infected stable cell lines were then fixed at
105 12hpi and immunofluorescent stained for ERGIC53 and co-stained with either SARS-CoV-2 S or N.
106 Images were captured by confocal microscopy and colocalization was assessed. HEK293T/hACE2 cells
107 stably expressing CNP showed higher colocalization between ERGIC and SARS-CoV-2 S as compared to
108 GFP control cells (Fig 2A, quantified in Fig 2C). However, colocalization between SARS-CoV-2 N and
109 ERGIC markers was markedly lower for CNP expressing cells as compared to GFP controls (Fig 2B,
110 quantified in Fig 2D), suggesting an inhibition of N trafficking to sites of virion assembly.
111
112 **CNP inhibits SARS-CoV-2-induced mitochondria depolarization.**
113 In order to assess the necessary aspects of CNP required for SARS-CoV-2 inhibition, HA-tagged
114 CNP or HA-tagged CNP mutation/deletion constructs were created, including constructs with mutations
115 to the known catalytic sites (H251A, T253A, H330A, T332A), prenylation site (C418A) and deletions of
116 the mitochondrial targeting sequence (Δ1-20) (S1B Fig, S2 Table). Other domain deletion constructs (i.e.,
117 Δ p-loop domain, Δ catalytic domain) were abandoned due to poor expression, likely caused by protein
118 misfolding (S1B Fig). Before analysis of their effect on infection, their localization was assayed in
119 transfected cells. The hCNP wildtype as well as the catalytic site and prenylation site mutant localize to
120 the mitochondria while the MTS deletion mutant is diffuse in the cytoplasm (S1C Fig). To determine the
121 domains of CNP required for SARS-CoV-2 inhibition, HEK293T/hACE2 cells were transfected with HA-
122 tagged wildtype and mutant CNP constructs. The day following transfections, cells were infected with
123 SARS-CoV-2/WA1 (MOI = 0.01) for 48 hours, at which point supernatants were collected and SARS-
124 CoV-2 titers determined by plaque assay. As shown previously, CNP overexpression resulted in a greater
125 than 10-fold decrease in SARS-CoV-2 titers as compared to GFP controls. However, deletion of the

126 mitochondrial targeting sequence resulted in ablation of SARS-CoV-2 inhibition, suggesting targeting of
127 CNP to mitochondria is required for antiviral activity (Fig 3A).
128 Given this result, we aimed to assess the effects of CNP overexpression on mitochondrial
129 function during SARS-CoV-2 infection. Previous work has shown that SARS-CoV-2 infection leads to
130 mPTP-induced mitochondrial depolarization as soon as 3hpi [39]. Additionally, others have shown that
131 CNP inhibits the formation and function of the mPTP [36, 37]. To further assess this relationship,
132 HEK293T/hACE2 cells were transfected with hCNP, hCNPΔMTS, or empty plasmid constructs as
133 described above and infected the following day with SARS-CoV-2/WA1 (MOI = 5). At 6hpi, cells were
134 stained with JC10 dye to assess mitochondrial depolarization or TMRM dye to assess mPTP opening. As
135 was shown previously, SARS-CoV-2 infection in control-transfected cells and hCNPΔMTS-transfected
136 cells led to mitochondrial depolarization, as shown by increases in JC10 staining (Fig 3B) and opening of
137 the mPTP as shown by loss of TMRM staining, as compared to mock infected cells. However, these
138 effects were not observed for hCNP-transfected cells, suggesting hCNP inhibits SARS-CoV-2-mediated
139 mitochondrial depolarization.
140 This data suggests that CNP could be directly regulating the mPTP opening and release of ROS. While
141 components of the mPTP are not agreed upon, the inhibition of mPTP opening by Cyclosporin A is. We
142 hypothesize that if hCNP is regulating mPTP opening then further inhibition by Cyclosporin A will not
143 cause additional reduction in virus titer. If however CNP is targeting a different process in the
144 mitochondria then the addition of Cyclosporin A before infection will additively or synergistically lead to
145 an increased inhibition of SARS-CoV-2 replication. To further assess the effects of hCNP on mPTP
146 function, HEK293T/hACE2 cells stably expressing either hCNP or GFP were infected with SARS-CoV-2
147 followed by treatment with 10μM Cyclosporin A, an established inhibitor of mPTP function, or DMSO as
148 a vehicle control. Intracellular SARS-CoV-2 titers were significantly lower when Cyclosporin A
149 treatment was administered to GFP stable cells but not lower for hCNP stable cells, as compared to
150 vehicle controls (Fig 3D). We conclude that this means that Cyclosporin A and hCNP could be targeting
151 the same complex in mitochondria, the mPTP.

152

153 **Mitochondrial reactive oxygen species release is needed for efficient SARS-CoV-2 virion assembly.**

154 We have confirmed that SARS-CoV-2 infection can induce mitochondrial dysfunction and
155 further show that this dysfunction can be inhibited by hCNP. One major consequence of sustained
156 mitochondrial depolarization is the production and release of ROS. To assess the importance of ROS to
157 SARS-CoV-2 virion assembly inhibition, HEK293T/hACE2 cells were transfected with hCNP,
158 hCNPΔMTS, the catalytic site mutant (hCNP/Cat), the prenylation site mutant (hCNP/Pren) or empty
159 plasmid constructs as described above and infected the following day with SARS-CoV-2/WA1 (MOI =
160 5). At 6hpi, cells were stained with H_2DCFDA to visualize cytosolic ROS (Fig 4A). As was shown
161 previously, SARS-CoV-2 infection in control-transfected cells and hCNPΔMTS-transfected cells led to
162 increased ROS production, as compared to mock infected cells. The hCNP/Cat mutant maintains
163 inhibition of ROS production after infection, similar to the wildtype hCNP. The hCNP/Pren mutation has
164 a moderate phenotype. The inhibition of ROS generation reflects the virus inhibition seen in Fig 3. This
165 data suggests that hCNP-inhibition of mitochondrial depolarization may lead to inhibition of ROS
166 production and release into the cytosol.

167 To further confirm the importance of ROS production to SARS-CoV-2 replication, we infected
168 HEK293/hACE2 cells stably expressing either hCNP or GFP with SARS-CoV-2/WA1 (MOI = 5) for a
169 45-minute absorption period followed by washing with cell culture media to remove any remaining
170 unbound virus. At 3hpi, cells were then treated with a sub-lethal concentration range of hydrogen
171 peroxide, one of the ROS released following mitochondrial depolarization, and intracellular/extracellular
172 SARS-CoV-2 titers assessed at 18hpi. The addition of ROS to hCNP-stable HEK293T/hACE2 cells
173 resulted in a dose-dependent rescue of SARS-CoV-2 titers as compared to GFP control cells when
174 assessed for intracellular (Fig 4B) or extracellular (Fig 4C) titers. This data suggests that ROS release
175 from the mitochondria is required for SARS-CoV-2 virion assembly and release.

176

177 **CNP reduces SARS-CoV-2 infection in a mouse model of COVID-19.**

178 To assess the effects of CNP on SARS-CoV-2 infection in a mouse model of COVID-19, rAd5
179 vectors were generated to dually express hACE2, the SARS-CoV-2 entry receptor, and either HA-tagged
180 hCNP or HA-tagged eGFP. To validate rAd5 transduction efficiency, Balb/c laboratory mice were
181 transduced intranasally with 1 x 10^8 viral particles (VP) per mouse and effects on weight change and
182 hCNP and hACE2 expression were assessed 3-days post-transduction (S3A Fig). rAd5 transduction
183 resulted in minimal weight-loss (S3B Fig) by 3-days post-transduction and we observed no qualitative
184 differences in pulmonary inflammation as shown by histology. Transduction by either rAd5 vector
185 resulted in increased expression of hACE2 (Fig 5c) and HA-tagged hCNP or HA-tagged eGFP (S3D Fig)
186 as visualized by immunofluorescent staining of lung histology sections. Additionally, levels of hACE2
187 mRNA were elevated due to either rAd5 transduction (Fig 5E) and hCNP mRNA was elevated in
188 rAd5/hCNP transduced animals (S3F Fig).
189 Using these validated rAd5 vectors, we next assessed effects of CNP on SARS-CoV-2 infection
190 in an animal COVID-19 disease model. Balb/c laboratory mice were intranasally transduced with rAd5
191 vectors (1 x 10^8 VP/mouse) 3 days-prior to intranasal challenge with SARS-CoV-2/WA1 (1 x 10^3
192 pfu/mouse or 1 x 10^5 pfu/mouse) (Fig 5A). Importantly, the WA1 strain of SARS-CoV-2 cannot enter
193 cells using murine ACE2 and will only be able to infect rAd5-transduced cells expressing hACE2. hCNP
194 overexpression resulted in a greater than 1000-fold decrease in live virus titers to undetectable levels from
195 mouse lung homogenates at 2- or 4-dpi for either the 1 x 10^3 pfu/mouse (Fig 5B) or 1 x 10^5 pfu/mouse
196 (Fig 5C) challenge groups. Additionally, there was a marked decrease in SARS-CoV-2 sgRNA in lungs
197 from hCNP transduced animals as compared to control animals for either 1 x 10^3 pfu/mouse (Fig 5D) or 1
198 x 10^5 pfu/mouse (Fig 5E) challenge groups.
199

200 ## Discussion

201 Therapeutics against COVID-19 remain limited to early SARS-CoV-2 replication cycle targets,
202 including monoclonal antibody treatments that block entry and nucleoside analogues that inhibit viral

203 RNA replication. This is in part due to the relative gap in understanding that remains for later SARS-
204 CoV-2 lifecycle stages. Our work aimed to further define the mechanism of action of a potential late-
205 stage inhibitor of SARS-CoV-2, CNP, to both assess its therapeutic potential and to further investigate
206 later SARS-CoV-2 lifecycle stages. Consistent with our previously published work, we confirmed that
207 CNP overexpression had no effect on SARS-CoV-2 genome replication but resulted in a significant
208 decrease in extracellular SARS-CoV-2 titers, again suggesting CNP inhibits somewhere between these
209 viral lifecycle steps. We further showed that the generation of sgRNA, the equivalent of the viral mRNA,
210 and translation of SARS-CoV-2 structural proteins were similarly not affected by CNP overexpression.
211 However, intracellular SARS-CoV-2 titers were significantly reduced in CNP overexpressing cells,
212 suggesting the generation of newly made virions is hampered in the presence of CNP. Indeed, CNP
213 overexpression resulted in a reduction of N localization to sites of virion assembly, the ERGIC, and
214 resulted in higher amounts of S localization at the ERGIC, suggesting unincorporated S may be
215 sequestered at the ERGIC awaiting assembly with N. Collectively, these data show that CNP inhibits the
216 assembly of new SARS-CoV-2 virions.

217 Our work also demonstrates the importance of mitochondrial depolarization to efficient virion
218 assembly. SARS-CoV-2 infection has been shown previously to lead to mitochondrial dysfunction and
219 the release of ROS, though no specific connection to viral replication was made [39]. Our study shows
220 that CNP targeting to mitochondria was essential for SARS-CoV-2 inhibition and that this targeting
221 decreased SARS-CoV-2-induced mitochondrial depolarization and ROS release. Interestingly, the
222 catalytic activity of CNP appeared to be somewhat dispensable for SARS-CoV-2 inhibition, suggesting
223 catalytic activity may not be required for mPTP inhibition, as has been suggested previously [36, 37].
224 Additionally, the inhibition of ROS production and release caused by mPTP opening appeared to be
225 driving SARS-CoV-2 inhibition, as the addition of ROS to infected CNP-expressing cells by peroxide
226 treatment rescued SARS-CoV-2 intracellular and extracellular titers. We also show that cyclosporin A
227 inhibits SARS-CoV-2 replication to the same level as CNP overexpression and together they show now
228 additional inhibition, suggesting they inhibit the same target. We hypothesize that if they altered different

229 targets then we would see an additive or synergistic effect on viral replication, which we do not. Further
230 research will be needed to assess how ROS release leads to more efficient virion assembly. It is possible
231 that cytosolic ROS may provide a more advantageous environment for post-translational modification to
232 SARS-CoV-2 structural proteins that regulate virion assembly, such as modifications to N that are
233 proposed to regulate N phase separation to promote virion assembly [40]. Alternatively, increases in ROS
234 signaling could promote virion assembly.

235 This study also shows the potential of CNP to be developed into a potent COVID-19 therapeutic.
236 Our mouse data shows that pre-treatment with CNP inhibited SARS-CoV-2 infection to below detectable
237 levels in lungs throughout the course of infection. Additionally, overexpression of CNP when
238 administered intranasally in mice showed no substantial side effects as measured by weight loss or
239 visualized by histology for pulmonary inflammation, suggesting a CNP treatment could be well tolerated.
240 Additionally, increases in systemic ROS during acute COVID-19 has been observed in humans and
241 implicated in the development of some "Long COVID" symptoms [41]. It is possible that CNP treatment
242 could alleviate some of these long-term effects. However, further development is needed to transition a
243 potential CNP treatment from rAd5 transduction to a more viable treatment option. Alternatively, other
244 mPTP inhibitors, such as Cyclosporin A, could show additional promise as a COVID-19 treatment *in vivo*
245 than what has already been demonstrated *in vitro* [39]. Collectively, this work shows the potential of
246 mPTP inhibition and reduction in ROS production as a treatment for COVID-19 and the potential of CNP
247 to be a new SARS-CoV-2 antiviral target.

248

249 # Material and Methods

250 **Data Availability**

251 All data for this manuscript is available at the Center for Open Science at https://osf.io/f6db3/

252

253 **Ethics Statement**

254 All experiments were approved by the University of Maryland at Baltimore, Institutional
255 Biosafety Committee and the Institutional Animal Care & Use Committee. All experiments with live
256 virus were performed in a biosafety level 3 facility at The University of Maryland at Baltimore.

257 **Cells**

258 VeroE6 cells overexpressing TMPRSS2 were generously provided by Dr. Makoto Takeda
259 (VeroT, [42]). VeroT and HEK293T cells overexpressing hACE2 (HEK293T/hACE2) (ATCC BEI NR-
260 52511) were cultured in DMEM medium (Quality Biological) supplemented with 10% (vol/vol) heat-
261 inactivated FBS (Sigma), 1% (vol/vol) penicillin–streptomycin (Gemini Bio-Products), 1% (vol/vol) l-
262 glutamine (2 mM final concentration; Gibco), and 1% (vol/vol) HEPES buffer (10mM final
263 concentration; Gibco).

264 **Virus**

265 All work with SARS-CoV-2 was performed in an A/BSL3 laboratory and approved by our
266 Institutional Biosafety Committee (IBC# IBC-00005484) and Institutional Animal Care and Use
267 Committee (IACUC# 1120004). The original strain of SARS-CoV-2 was provided by the CDC following
268 isolation from a patient in Washington State (WA-1; BEI number NR-52281). Formal consent was
269 obtained for sampling via the CDC. Stocks were prepared by infection of VeroT cells for two days when
270 a cytopathic effect was starting to become visible. The media were collected and clarified by
271 centrifugation before being aliquoted for storage at −80 °C. The titer of the stock was determined by
272 plaque assay using VeroT cells.

273 Lentiviruses and adenoviruses were purchased from and prepared by VectorBuilder Inc. Any
274 infections with lentiviruses and adenoviruses were performed in an A/BSL2 or A/BSL3 laboratory and
275 approved by our Institutional Biosafety Committee (IBC# IBC-00005484) and Institutional Animal Care
276 and Use Committee (IACUC# 1120004).

277 **Semi-solid Avicel Plaque Assay**

278 Plaque assays were performed similar to what has been described previously [43]. Briefly, 12-
279 well plates were seeded with 2.5 x 10^5 VeroT cells/well one day prior to processing. On the day of

280 processing, media was removed from the 12-well plates and 200µL of dilutions of sample in DMEM were
281 added to each well. Plates were incubated at 37 °C (5% CO_2) for 1 hour with rocking every 15 minutes.
282 Following incubation, 2mL of plaque assay media, DMEM containing 0.1% agarose (UltraPure) and 2%
283 FBS (Gibco), was added to each well and incubated for 2 days at 37 °C (5% CO_2). Following incubation,
284 plates were fixed with 4% paraformaldehyde, stained with 0.25% crystal violet (w/v), plaques counted,
285 and titers calculated as plaque forming units (PFU).

286 **RT-qPCR**

287 RT-qPCR was processed for cell lysate and for mouse lung homogenates as described previously
288 [43]. RNA was extracted per the manufacturer's instructions using the Direct-zol RNA Miniprep Kit
289 (Zymo Research). RNA was converted into cDNA (Thermo RevertAid Reverse Transcriptase) and used
290 as template for qPCR (Qiagen RT2 SYBR green qPCR Mastermix). Primers are listed in S1 Table. Data
291 was collected on a 7500 Fast Dx Real-Time PCR Instrument (Applied Biosystems).

292 **Plasmids**

293 Full length, domain deletion, and functional mutation human CNP gene versions were cloned into
294 a pCAGGS-HA as described previously [44]. Briefly, genes were cloned into pCAGGS-HA vectors on
295 EcoR1/Xma1 sites, resulting in a C-terminal HA epitope tag. Genes or gene fragments were PCR
296 amplified with primers (S2 Table) to allow for In-Fusion gene cloning (Takara Bio) according to the
297 manufacturer's instructions. For functional mutant clones, primer directed mutagenesis was performed
298 and gene fragments were combined during the In-fusion cloning process.

299 **SARS-CoV-2 inhibition by CNP deletion/mutation constructs**

300 All CNP-mediated SARS-CoV-2 inhibition analysis was performed using HEK293T/hACE2
301 cells. HEK293T/hACE2 cells were seeded in 24-well plates pre-coated with 50µg/mL Rat Tail Collagen I
302 (Gibco), according to the manufacturer's instructions. At the time of seeding, pCAGGS-HA plasmids
303 were transfected using 1µL TransIT 2020 (Mirus) per 100µg plasmid and incubated overnight. Cells were
304 then infected with SARS-CoV-2/WA1 (MOI = 0.01). Supernatants were collected 48-hours post-infection
305 and SARS-CoV-2 titers determined by VeroT plaque assay.

306 **Stable Cell Line Generation**

307 Lentiviruses expressing HA-tagged CNP or HA-tagged GFP were obtained from VectorBuilder,
308 Inc. HEK293T/hACE2 cells were transduced with lentiviruses (MOI = 3) pre-treated with 10µg/mL
309 Polybrene (VectorBuilder, Inc.). Transduced cells were selected by resistance to 10µg/mL Blasticidin
310 (InvivoGen) for 10 days, followed by continued maintenance in cell culture media supplemented with
311 10µg/mL Blasticidin (InvivoGen).

312 **SARS-CoV-2 Lifecycle Inhibition Analysis**

313 HEK293T/hACE2 cells stably expressing CNP/HA or GFP/HA were seeded in 24-well plates
314 pre-coated with 50µg/mL Rat Tail Collagen I (Gibco), according to the manufacturer's instructions, or in
315 Tab-Tek II CC2 chamber slides (Thermo Fisher Scientific). Separate wells were seeded for each assay to
316 process. The following day, cells were infected with SARS-CoV-2/WA1 (MOI = 5) for a 45-minute
317 absorption period, followed by inoculum removal and washing with fresh cell culture media. Cells were
318 then maintained at cell culture conditions until collection.

319 At 6-hours post infection, cells were washed with complete cell culture media and then lysed in
320 TRIzol (Ambion). Lysates were stored at -80°C until processing for RT-qPCR.

321 At 12-hours post-infection, cells were washed with complete cell culture media and then lysed in
322 complete lysis buffer containing 20mM Tris-HCl, 150mM NaCl, 1% Nonidet P-40 (v/v), 0.5% Sodium
323 Dodecyl Sulphate (w/v), 5mM EDTA, and 1 X complete protease inhibitor (Roche), for 5 minutes at
324 room temperature. Lysates were collected and then boiled twice at 95°C for 30 minutes. Lysates were
325 then centrifuged at 21,000 x g for 20 minutes followed by supernatant collection. Supernatants were and
326 stored at -80°C until ready to process by Western Blot (below).

327 At 12-hours post-infection, cells were fixed in 2% paraformaldehyde for 1 hour at 4°C and then
328 washes once with 1 x PBS. Fixed cells were stored at 4°C until processing for immunofluorescent
329 microscopy and confocal microscopy.

330 At 18-hours post-infection, supernatants were collected for extracellular SARS-CoV-2 titer
331 determination and stored at -80°C until VeroT plaque assay processing. Cells were then washed once with

332 complete cell culture media followed by addition of 120µL of complete cell culture media. Cells were
333 then freeze-thawed three times to burst cells and lysates were collected for intracellular SARS-CoV-2 titer
334 determination and stored at -80°C until VeroT plaque assay processing.

335 **Western Blot**

336 Western blots were performed similar to what has been described previously [45]. Cell lysates
337 were run on Mini-PROTEAN TGX Precast Gels (BioRad) and tank blotted onto PVDF membranes
338 according to the manufacturer's instructions. Following blotting, membranes were blocked in blocking
339 buffer, TBST (TBS (from where?) with 0.1% Tween 20 (v/v) (from where)) and 5% milk (w/v) (from
340 where), for 1 hour at room temperature. Membranes were then incubated in primary antibody overnight at
341 4°C followed by 3 x 10-minute washes with TBST. Membranes were then incubated with diluted
342 secondary antibodies for 1 hour at room temperature followed by 5 x 10-minute washes with TBST.
343 Membranes were then developed with ECL (Cytiva) and imaged with a CCD camera. All antibodies (S3
344 Table) were diluted in blocking buffer.

345 **Immunofluorescence Microscopy and Confocal Microscopy**

346 Paraformaldehyde fixed cells were permeabilized in PBS with 0.3% Triton-100 for 30 minutes at
347 room temperature. Cells were then blocked in blocking buffer, PBS containing 5% BSA (w/v), for 1 hour
348 at room temperature. Cells were then incubated with diluted primary antibody overnight at 4°C followed
349 by 3 x 10-minute washes with wash buffer, PBS containing 1% BSA (w/v) and 0.1% Tween-20 (v/v).
350 Cells were then incubated with diluted secondary antibodies for 1 hour at room temperature followed by 3
351 x 10-minute washes with wash buffer and 2 x 10-minute washes in PBS. Coverslips were then mounted
352 with ProLong Glass Antifade Mountant with NucBlue (Invitrogen) for at least 30 minutes at room
353 temperature. All antibodies (S3 Table) were diluted in blocking buffer.

354 Stained slides were visualized using a Revolve fluorescent microscope (Echo) or a W-1 Spinning
355 Disk confocal microscope (Nikon). Images collected by confocal microscopy were 2-D deconvoluted
356 using the W-1 spinning disk software and analyzed with ImageJ (NIH) using the Colocalization
357 Threshold colocalization plugin. At least 100 cells per condition were analyzed for colocalization

358 determination in three separate image fields and the percent intensity above threshold colocalized for
359 SARS-CoV-2 S or N with ERGIC53 are reported. Data are representative of two independent
360 experiments.

361 **Mitochondrial Function Assay Design**

362 HEK293T/hACE2 cells were seeded in Tab-Tek II CC2 chamber slides (Thermo Fisher
363 Scientific). At the time of seeding, pCAGGS-HA plasmids were transfected using 1µL TransIT 2020
364 (Mirus) per 100µg plasmid and maintained at cell culture conditions overnight. Cells were then infected
365 with SARS-CoV-2/WA1 (MOI = 0.1). Mitochondrial function assays (described below) were then
366 processed at 6-hours post-infection.

367 **JC-10 Staining**

368 At 6-hours post-infection, JC-10 staining was completed using the mitochondria membrane
369 potential kit (Sigma-Aldrich) according to the manufacturer's instructions. Slides were then washed once
370 with 1 x HBBS and fixed in 2% paraformaldehyde for 30 minutes at room temperature. Coverslips were
371 then mounted with ProLong Glass Antifade Mountant with NucBlue (Invitrogen) for 30 minutes at room
372 temperature and visualized immediately using a Revolve fluorescent microscope (Echo).

373 **TMRM Staining**

374 At 6-hours post-infection, opening of the mitochondrial permeabilization transition pore (mPTP)
375 was visualized by tetramethylrhodamine methyl ester perchlorate (TMRM) staining (Sigma). Cells were
376 washed once with 1 x HBBS (Gibco) followed by incubation with 100 nM TMRM diluted in 1 x HBBS
377 for 30 minutes at 37°C. Slides were then washed once with 1 x PBS and fixed in 2% paraformaldehyde
378 for 30 minutes at room temperature. Coverslips were then mounted with ProLong Glass Antifade
379 Mountant with NucBlue (Invitrogen) for 30 minutes at room temperature and visualized immediately
380 using a Revolve fluorescent microscope (Echo).

381 **Reactive Oxygen Species Staining (H2DCFDA)**

382 At 6-hours post-infection, intracellular reactive oxygen species levels were visualized by
383 H_2DCFDA staining (Invitrogen) according to the manufacturer's instructions. Briefly, cells were washed

384 twice with 1 x HBBS (Gibco) followed by incubation with 2.5µM H_2DCFDA diluted in 1 x HBBS for 30
385 minutes at 37°C. Slides were then washed three times with 1 x PBS and fixed in 2% paraformaldehyde
386 for 30 minutes at room temperature. Cells were visualized immediately using a Revolve fluorescent
387 microscope (Echo).

388 **Reactive oxygen species Addition and Cyclosporin-A Treatment Experiments**

389 HEK293T/hACE2 cells stably expressing either CNP/HA or GFP/HA were seeded and infected
390 with SARS-CoV-2/WA1 as described in "SARS-CoV-2 Lifecycle Inhibition Analysis". At 3-hours post-
391 infection, a concentration range of hydrogen peroxide (Sigma Aldrich) or vehicle (water) was added to
392 infected cells. At 18-hours post infection, supernatants and cell lysates were collected for
393 extracellular/intracellular SARS-CoV-2 titer determination as described in "SARS-CoV-2 Lifecycle
394 Inhibition Analysis" and stored at -80°C until further processing.

395 For Cyclosporin A treatment studies, HEK293T/hACE2 cells stably expressing either CNP/HA or
396 GFP/HA were seeded and infected with SARS-CoV-2/WA1 as described in "SARS-CoV-2 Lifecycle
397 Inhibition Analysis". After washing away unbound virus, fresh media containing 10µM Cyclosporin A
398 (SelleckChem) or 0.01% DMSO as a vehicle control was added to cells. At 18-hours post infection, cell
399 lysates were collected for intracellular SARS-CoV-2 titer determination as described in "SARS-CoV-2
400 Lifecycle Inhibition Analysis" and stored at -80°C until further processing.

401 **CNP overexpression antiviral Testing *in vivo***

402 Two mammalian gene expression recombinant Adenovirus serotype 5 (rAd5) viral vectors were
403 prepared by and obtained from VectorBuilder Inc. to dually express hACE2 and either: (1) HA-tagged
404 hCNP (Ad/CNP); or (2) HA-tagged enhanced green fluorescent protein (Ad/eGFP). To confirm rAd5
405 transduction, 8-10 week old BALB/c laboratory mice were anaesthetized with a mix of xylazine and
406 ketamine diluted in phosphate buffered saline prior to intranasal transduction with 1 x 10^8 PFU of either
407 Ad/CNP or Ad/eGFP and weights were recorded (Fig 5A). At 3-days post-rAd5-transduction, weights
408 were again recorded and lungs harvested and sectioned for the following: (1) fixed in 4%
409 paraformaldehyde for histopathological analysis and immunofluorescent staining; and (2) homogenized in

410 TRIzol for RT-qPCR analysis. Homogenization occurred using 1.0 mm glass beads (Sigma Aldrich) and
411 a Beadruptor (Omni International Inc.).
412 For SARS-CoV-2 antiviral testing, 8-10 week old BALB/c laboratory mice were anaesthetized
413 with a mix of xylazine and ketamine diluted in phosphate buffered saline prior to intranasal transduction
414 with 1 x 10^8 PFU of either Ad/CNP or Ad/eGFP. Three days later, mice were again anaesthetized with a
415 mix of xylazine and ketamine diluted in phosphate buffered saline prior to intranasal inoculation with
416 either 1 x 10^3 PFU or 1 x 10^5 PFU of SARS-CoV-2/WA1 (Fig 6A). Control mice were also mock infected
417 with 1 x PBS. Weights were collected daily following SARS-CoV-2 infection and 5 mice sacrificed on 2
418 dpi and 4 dpi for each treatment group. Lungs were harvested and sectioned for the following: (1) fixed in
419 4% paraformaldehyde for histopathological analysis; (2) homogenized in TRIzol for RT-qPCR analysis;
420 and (3) homogenized in PBS for plaque assay processing. Homogenization occurred using 1.0 mm glass
421 beads (Sigma Aldrich) and a Beadruptor (Omni International Inc.).

422 **Histopathology**

423 Histopathology was processed as described previously [46]. Lung sections were fixed in 4%
424 paraformaldehyde in phosphate-buffered saline for a minimum of 48 h, after which they were sent to the
425 Histology Core at the University of Maryland, Baltimore, for paraffin embedding and sectioning. Five-
426 micrometer sections were prepared and used for hematoxylin and eosin (H&E) staining by the Histology
427 Core Services. Sections were imaged at 10x magnification and assembled into figures using Adobe
428 Photoshop and Illustrator software.

429 **Immunofluorescent staining of mouse lung histology slides**

430 Lung sections were fixed in 4% paraformaldehyde in phosphate-buffered saline for a minimum of
431 48 h, after which they were sent to the Histology Core at the University of Maryland, Baltimore, for
432 paraffin embedding and sectioning. Slides were then deparaffinized with 2 x 5-minute washes in Xylenes
433 (Sigma Aldrich) followed by rehydration with decreasing concentrations of ethanol in water. Following
434 rehydration, antigen retrieval was completed by boiling samples in citrate buffer (Millipore Sigma) for 5

435 minutes followed with removal of heat and an additional 15-minute incubation. Samples were then
436 washed twice with ddH2O.
437 Slides were then stained for immunofluorescent imaging. All incubations were performed in a humidified
438 chamber. Slides were blocked in blocking buffer, PBS++ (1 x PBS with 1mM MgCl and 1mM $CaCl_2$)
439 with 1% (w/v) BSA, for 1 hour at room temperature. Following blocking, slides were incubated overnight
440 at 4°C with diluted primary antibody followed by 3 x 10-minute washes with PBS++. Slides were then
441 incubated for 1 hour at room temperature with diluted secondary antibodies, followed by 3 x 10-minute
442 washes with PBS++. Coverslips were then mounted with ProLong Glass Antifade Mountant with
443 NucBlue (Invitrogen) for at least 30 minutes at room temperature and visualized using a Revolve
444 fluorescent microscope (Echo). All antibodies (S3 Table) were diluted in blocking buffer.
445

446 **Acknowledgements**

447 The authors would like to thank the Histology Core at the University of Maryland, Baltimore for
448 histology processing.
449

450 **Funding**

451 This work is partially funded by NIH R01 AI148166 (to MBF). The funders had no role in study design,
452 data collection and analysis, decision to publish, or preparation of the manuscript.
453

454 **Contributions**

455 Conceptualization: J.L., M.B.F. Investigation: J.L., V.M.M., J.A., and M.B.F. Writing – Original Draft
456 Preparation: J.L., V.M.M, and J.A. Writing – Review & Editing: J.L., V.M.M., J.A., and M.B.F.
457

458 **Competing Interests Statement**

459 M.B.F. is on the scientific advisory board of Aikido Pharma and has collaborative research agreements
460 with Novavax, AstraZeneca, Regeneron, and Irazu Bio. These do not have any effect on the planning or
461 interpretations of the work presented in this manuscript.
462

463 **References**

464 1. Huang C, Wang Y, Li X, Ren L, Zhao J, Hu Y, et al. Clinical features of patients infected with
465 2019 novel coronavirus in Wuhan, China. Lancet. 2020;395(10223):497-506. Epub 2020/01/28. doi:
466 10.1016/s0140-6736(20)30183-5. PubMed PMID: 31986264.
467 2. Zhou P, Yang XL, Wang XG, Hu B, Zhang L, Zhang W, et al. A pneumonia outbreak associated
468 with a new coronavirus of probable bat origin. Nature. 2020;579(7798):270-3. Epub 2020/02/06. doi:
469 10.1038/s41586-020-2012-7. PubMed PMID: 32015507; PubMed Central PMCID: PMCPMC7095418.
470 3. Zhu N, Zhang D, Wang W, Li X, Yang B, Song J, et al. A Novel Coronavirus from Patients with
471 Pneumonia in China, 2019. N Engl J Med. 2020;382(8):727-33. Epub 2020/01/25. doi:
472 10.1056/NEJMoa2001017. PubMed PMID: 31978945; PubMed Central PMCID: PMCPMC7092803.
473 4. Dong E, Du H, Gardner L. An interactive web-based dashboard to track COVID-19 in real time.
474 Lancet Infect Dis. 2020;20(5):533-4. Epub 2020/02/23. doi: 10.1016/s1473-3099(20)30120-1. PubMed
475 PMID: 32087114; PubMed Central PMCID: PMCPMC7159018.
476 5. Dong E, Du H, Gardner L. COVID-19 Dashboard 2020 [cited 2023 March 02]. Available from:
477 https://coronavirus.jhu.edu/map.html.
478 6. Dittmar M, Lee JS, Whig K, Segrist E, Li M, Kamalia B, et al. Drug repurposing screens reveal
479 cell-type-specific entry pathways and FDA-approved drugs active against SARS-Cov-2. Cell Rep.
480 2021;35(1):108959. Epub 2021/04/04. doi: 10.1016/j.celrep.2021.108959. PubMed PMID: 33811811;
481 PubMed Central PMCID: PMCPMC7985926.
482 7. Riva L, Yuan S, Yin X, Martin-Sancho L, Matsunaga N, Pache L, et al. Discovery of SARS-
483 CoV-2 antiviral drugs through large-scale compound repurposing. Nature. 2020;586(7827):113-9. Epub

484 2020/07/25. doi: 10.1038/s41586-020-2577-1. PubMed PMID: 32707573; PubMed Central PMCID:
485 PMCPMC7603405.
486 8. Weston S, Coleman CM, Haupt R, Logue J, Matthews K, Li Y, et al. Broad Anti-coronavirus
487 Activity of Food and Drug Administration-Approved Drugs against SARS-CoV-2 In Vitro and SARS-
488 CoV In Vivo. J Virol. 2020;94(21). Epub 2020/08/21. doi: 10.1128/jvi.01218-20. PubMed PMID:
489 32817221; PubMed Central PMCID: PMCPMC7565640.
490 9. FDA. FDA Approves First Treatment for COVID-19 2020 [cited 2023 MARCH 7]. Available
491 from: https://www.fda.gov/news-events/press-announcements/fda-approves-first-treatment-covid-19.
492 10. FDA. Lagevrio (molnupiravir) Letter of Authorization 2022. Available from:
493 https://www.fda.gov/media/155053/download.
494 11. FDA. Paxlovid (nirmatrelvir tablets and ritonavir tablets, co-packaged for oral use) Letter of
495 Authorization 2022 [cited 2023 MARCH 7]. Available from:
496 https://www.fda.gov/media/155049/download.
497 12. FDA. Bamlanivimab and Etesevimab Letter of Authhorization 2022 [cited 2023 MARCH 7].
498 Available from: https://www.fda.gov/media/145801/download.
499 13. FDA. Evusheld (tixagevimab co-packaged with cilgavimab) Letter of Authorization 2022 [cited
500 2023 MARCH 7]. Available from: https://www.fda.gov/media/154704/download.
501 14. FDA. Sotrovimab Letter of Authorization 2022 [cited 2023 MARCH 7]. Available from:
502 https://www.fda.gov/media/149532/download.
503 15. Belouzard S, Chu VC, Whittaker GR. Activation of the SARS coronavirus spike protein via
504 sequential proteolytic cleavage at two distinct sites. Proc Natl Acad Sci U S A. 2009;106(14):5871-6.
505 Epub 2009/03/27. doi: 10.1073/pnas.0809524106. PubMed PMID: 19321428; PubMed Central PMCID:
506 PMCPMC2660061.
507 16. Gierer S, Bertram S, Kaup F, Wrensch F, Heurich A, Krämer-Kühl A, et al. The spike protein of
508 the emerging betacoronavirus EMC uses a novel coronavirus receptor for entry, can be activated by

509 TMPRSS2, and is targeted by neutralizing antibodies. J Virol. 2013;87(10):5502-11. Epub 2013/03/08.
510 doi: 10.1128/jvi.00128-13. PubMed PMID: 23468491; PubMed Central PMCID: PMCPMC3648152.
511 17. Hoffmann M, Kleine-Weber H, Schroeder S, Krüger N, Herrler T, Erichsen S, et al. SARS-CoV-
512 2 Cell Entry Depends on ACE2 and TMPRSS2 and Is Blocked by a Clinically Proven Protease Inhibitor.
513 Cell. 2020;181(2):271-80.e8. Epub 2020/03/07. doi: 10.1016/j.cell.2020.02.052. PubMed PMID:
514 32142651; PubMed Central PMCID: PMCPMC7102627.
515 18. Letko M, Marzi A, Munster V. Functional assessment of cell entry and receptor usage for SARS-
516 CoV-2 and other lineage B betacoronaviruses. Nat Microbiol. 2020;5(4):562-9. Epub 2020/02/26. doi:
517 10.1038/s41564-020-0688-y. PubMed PMID: 32094589; PubMed Central PMCID: PMCPMC7095430.
518 19. Matsuyama S, Nagata N, Shirato K, Kawase M, Takeda M, Taguchi F. Efficient activation of the
519 severe acute respiratory syndrome coronavirus spike protein by the transmembrane protease TMPRSS2. J
520 Virol. 2010;84(24):12658-64. Epub 2010/10/12. doi: 10.1128/jvi.01542-10. PubMed PMID: 20926566;
521 PubMed Central PMCID: PMCPMC3004351.
522 20. Ou X, Liu Y, Lei X, Li P, Mi D, Ren L, et al. Characterization of spike glycoprotein of SARS-
523 CoV-2 on virus entry and its immune cross-reactivity with SARS-CoV. Nat Commun. 2020;11(1):1620.
524 Epub 2020/03/30. doi: 10.1038/s41467-020-15562-9. PubMed PMID: 32221306; PubMed Central
525 PMCID: PMCPMC7100515.
526 21. Walls AC, Park YJ, Tortorici MA, Wall A, McGuire AT, Veesler D. Structure, Function, and
527 Antigenicity of the SARS-CoV-2 Spike Glycoprotein. Cell. 2020;181(2):281-92.e6. Epub 2020/03/11.
528 doi: 10.1016/j.cell.2020.02.058. PubMed PMID: 32155444; PubMed Central PMCID:
529 PMCPMC7102599.
530 22. Chan JF, Kok KH, Zhu Z, Chu H, To KK, Yuan S, et al. Genomic characterization of the 2019
531 novel human-pathogenic coronavirus isolated from a patient with atypical pneumonia after visiting
532 Wuhan. Emerg Microbes Infect. 2020;9(1):221-36. Epub 2020/01/29. doi:
533 10.1080/22221751.2020.1719902. PubMed PMID: 31987001; PubMed Central PMCID:
534 PMCPMC7067204.

535 23. Finkel Y, Mizrahi O, Nachshon A, Weingarten-Gabbay S, Morgenstern D, Yahalom-Ronen Y, et
536 al. The coding capacity of SARS-CoV-2. Nature. 2021;589(7840):125-30. Epub 2020/09/10. doi:
537 10.1038/s41586-020-2739-1. PubMed PMID: 32906143.
538 24. Snijder EJ, Limpens R, de Wilde AH, de Jong AWM, Zevenhoven-Dobbe JC, Maier HJ, et al. A
539 unifying structural and functional model of the coronavirus replication organelle: Tracking down RNA
540 synthesis. PLoS Biol. 2020;18(6):e3000715. Epub 2020/06/09. doi: 10.1371/journal.pbio.3000715.
541 PubMed PMID: 32511245; PubMed Central PMCID: PMCPMC7302735.
542 25. Wolff G, Limpens R, Zevenhoven-Dobbe JC, Laugks U, Zheng S, de Jong AWM, et al. A
543 molecular pore spans the double membrane of the coronavirus replication organelle. Science.
544 2020;369(6509):1395-8. Epub 2020/08/09. doi: 10.1126/science.abd3629. PubMed PMID: 32763915;
545 PubMed Central PMCID: PMCPMC7665310.
546 26. Viehweger A, Krautwurst S, Lamkiewicz K, Madhugiri R, Ziebuhr J, Hölzer M, et al. Direct
547 RNA nanopore sequencing of full-length coronavirus genomes provides novel insights into structural
548 variants and enables modification analysis. Genome Res. 2019;29(9):1545-54. Epub 2019/08/24. doi:
549 10.1101/gr.247064.118. PubMed PMID: 31439691; PubMed Central PMCID: PMCPMC6724671.
550 27. de Haan CA, Rottier PJ. Molecular interactions in the assembly of coronaviruses. Adv Virus Res.
551 2005;64:165-230. Epub 2005/09/06. doi: 10.1016/s0065-3527(05)64006-7. PubMed PMID: 16139595;
552 PubMed Central PMCID: PMCPMC7112327.
553 28. Klein S, Cortese M, Winter SL, Wachsmuth-Melm M, Neufeldt CJ, Cerikan B, et al. SARS-CoV-
554 2 structure and replication characterized by in situ cryo-electron tomography. Nat Commun.
555 2020;11(1):5885. Epub 2020/11/20. doi: 10.1038/s41467-020-19619-7. PubMed PMID: 33208793;
556 PubMed Central PMCID: PMCPMC7676268.
557 29. Stertz S, Reichelt M, Spiegel M, Kuri T, Martínez-Sobrido L, García-Sastre A, et al. The
558 intracellular sites of early replication and budding of SARS-coronavirus. Virology. 2007;361(2):304-15.
559 Epub 2007/01/11. doi: 10.1016/j.virol.2006.11.027. PubMed PMID: 17210170; PubMed Central PMCID:
560 PMCPMC7103305.

561 30. Martin-Sancho L, Lewinski MK, Pache L, Stoneham CA, Yin X, Becker ME, et al. Functional
562 landscape of SARS-CoV-2 cellular restriction. Mol Cell. 2021;81(12):2656-68.e8. Epub 2021/05/01. doi:
563 10.1016/j.molcel.2021.04.008. PubMed PMID: 33930332; PubMed Central PMCID: PMCPMC8043580.
564 31. de Monasterio-Schrader P, Jahn O, Tenzer S, Wichert SP, Patzig J, Werner HB. Systematic
565 approaches to central nervous system myelin. Cell Mol Life Sci. 2012;69(17):2879-94. Epub 2012/03/24.
566 doi: 10.1007/s00018-012-0958-9. PubMed PMID: 22441408.
567 32. Rösener M, Muraro PA, Riethmüller A, Kalbus M, Sappler G, Thompson RJ, et al. 2',3'-cyclic
568 nucleotide 3'-phosphodiesterase: a novel candidate autoantigen in demyelinating diseases. J
569 Neuroimmunol. 1997;75(1-2):28-34. Epub 1997/05/01. doi: 10.1016/s0165-5728(96)00230-5. PubMed
570 PMID: 9143234.
571 33. Uhlén M, Fagerberg L, Hallström BM, Lindskog C, Oksvold P, Mardinoglu A, et al. Proteomics.
572 Tissue-based map of the human proteome. Science. 2015;347(6220):1260419. Epub 2015/01/24. doi:
573 10.1126/science.1260419. PubMed PMID: 25613900.
574 34. Drummond GI, Perrott-Yee S. Enzymatic hydrolysis of adenosine 3',5'-phosphoric acid. J Biol
575 Chem. 1961;236:1126-9. Epub 1961/04/01. PubMed PMID: 13724509.
576 35. Azarashvili T, Krestinina O, Galvita A, Grachev D, Baburina Y, Stricker R, et al. Ca2+-
577 dependent permeability transition regulation in rat brain mitochondria by 2',3'-cyclic nucleotides and 2',3'-
578 cyclic nucleotide 3'-phosphodiesterase. Am J Physiol Cell Physiol. 2009;296(6):C1428-39. Epub
579 2009/04/10. doi: 10.1152/ajpcell.00006.2009. PubMed PMID: 19357238.
580 36. Baburina Y, Azarashvili T, Grachev D, Krestinina O, Galvita A, Stricker R, et al. Mitochondrial
581 2', 3'-cyclic nucleotide 3'-phosphodiesterase (CNP) interacts with mPTP modulators and functional
582 complexes (I-V) coupled with release of apoptotic factors. Neurochem Int. 2015;90:46-55. Epub
583 2015/07/19. doi: 10.1016/j.neuint.2015.07.012. PubMed PMID: 26188334.
584 37. Baburina Y, Odinokova I, Azarashvili T, Akatov V, Lemasters JJ, Krestinina O. 2',3'-Cyclic
585 nucleotide 3'-phosphodiesterase as a messenger of protection of the mitochondrial function during
586 melatonin treatment in aging. Biochim Biophys Acta Biomembr. 2017;1859(1):94-103. Epub 2016/11/12.

587 doi: 10.1016/j.bbamem.2016.11.003. PubMed PMID: 27836641; PubMed Central PMCID:
588 PMCPMC5539527.
589 38. McFerran B, Burgoyne R. 2',3'-Cyclic nucleotide 3'-phosphodiesterase is associated with
590 mitochondria in diverse adrenal cell types. J Cell Sci. 1997;110 (Pt 23):2979-85. Epub 1998/02/07. doi:
591 10.1242/jcs.110.23.2979. PubMed PMID: 9359886.
592 39. Shang C, Liu Z, Zhu Y, Lu J, Ge C, Zhang C, et al. SARS-CoV-2 Causes Mitochondrial
593 Dysfunction and Mitophagy Impairment. Front Microbiol. 2021;12:780768. Epub 2022/01/25. doi:
594 10.3389/fmicb.2021.780768. PubMed PMID: 35069483; PubMed Central PMCID: PMCPMC8770829.
595 40. Lu S, Ye Q, Singh D, Cao Y, Diedrich JK, Yates JR, 3rd, et al. The SARS-CoV-2 nucleocapsid
596 phosphoprotein forms mutually exclusive condensates with RNA and the membrane-associated M
597 protein. Nat Commun. 2021;12(1):502. Epub 2021/01/23. doi: 10.1038/s41467-020-20768-y. PubMed
598 PMID: 33479198; PubMed Central PMCID: PMCPMC7820290.
599 41. Kell DB, Pretorius E. The potential role of ischaemia-reperfusion injury in chronic, relapsing
600 diseases such as rheumatoid arthritis, Long COVID, and ME/CFS: evidence, mechanisms, and
601 therapeutic implications. Biochem J. 2022;479(16):1653-708. Epub 2022/09/01. doi:
602 10.1042/bcj20220154. PubMed PMID: 36043493; PubMed Central PMCID: PMCPMC9484810.
603 42. Matsuyama S, Nao N, Shirato K, Kawase M, Saito S, Takayama I, et al. Enhanced isolation of
604 SARS-CoV-2 by TMPRSS2-expressing cells. Proc Natl Acad Sci U S A. 2020;117(13):7001-3. Epub
605 2020/03/14. doi: 10.1073/pnas.2002589117. PubMed PMID: 32165541; PubMed Central PMCID:
606 PMCPMC7132130.
607 43. Coleman CM, Frieman MB. Growth and Quantification of MERS-CoV Infection. Curr Protoc
608 Microbiol. 2015;37(1):15e.2.1-9. Epub 2015/09/08. doi: 10.1002/9780471729259.mc15e02s37. PubMed
609 PMID: 26344219; PubMed Central PMCID: PMCPMC4735735.
610 44. Weston S, Baracco L, Keller C, Matthews K, McGrath ME, Logue J, et al. The SKI complex is a
611 broad-spectrum, host-directed antiviral drug target for coronaviruses, influenza, and filoviruses. Proc Natl

612 Acad Sci U S A. 2020;117(48):30687-98. Epub 2020/11/14. doi: 10.1073/pnas.2012939117. PubMed
613 PMID: 33184176; PubMed Central PMCID: PMCPMC7720140.
614 45. Weston S, Matthews KL, Lent R, Vlk A, Haupt R, Kingsbury T, et al. A Yeast Suppressor Screen
615 Used To Identify Mammalian SIRT1 as a Proviral Factor for Middle East Respiratory Syndrome
616 Coronavirus Replication. J Virol. 2019;93(16). Epub 2019/05/31. doi: 10.1128/jvi.00197-19. PubMed
617 PMID: 31142674; PubMed Central PMCID: PMCPMC6675885.
618 46. Schultz DC, Johnson RM, Ayyanathan K, Miller J, Whig K, Kamalia B, et al. Pyrimidine
619 inhibitors synergize with nucleoside analogues to block SARS-CoV-2. Nature. 2022;604(7904):134-40.
620 Epub 2022/02/08. doi: 10.1038/s41586-022-04482-x. PubMed PMID: 35130559.
621
622

623 Figure Legends

624 **Fig 1: CNP overexpression inhibits generation of new SARS-CoV-2 virions.**
625 HEK293T/hACE2 cells stably overexpressing either CNP or GFP were infected with SARS-CoV-2/WA1
626 for 45-minutes followed by washing of any unbound virus. At 6-hours post-infection, intracellular SARS-
627 CoV-2 RNA levels were determined by RT-qPCR for (**a**) genomic RNA and (**b**) subgenomic RNA. (**c**) At
628 12-hours post-infection, lysates were collected and western blot staining performed for SARS-CoV-2 S,
629 SARS-CoV-2 N, and actin as a loading control. At 18-hours post-infection, plaque assays were performed
630 to determine (**d**) intracellular SARS-CoV-2 titers and (**e**) extracellular SARS-CoV-2 titers. All
631 experiments were repeated 2-3 times, as noted by the points in the figure. **$p \leq 0.01$, ***$p \leq 0.001$, "ns":
632 $p > 0.5$.
633

634 **Fig 2: CNP overexpression alters SARS-CoV-2 structural protein localization during virion**
635 **assembly.**

636 HEK293T/hACE2 cells stably overexpressing either CNP or GFP were infected with SARS-CoV-2/WA1
637 for 45-minutes followed by washing of any unbound virus. At 12-hours post infection, cells were fixed,
638 immunofluorescent stained, and confocal images collected for (**a**) ERGIC53 (blue) and SARS-CoV-2 S
639 (red) or (**b**) ERGIC53 (blue) and SARS-CoV-2 N (red). ERGIC53 colocalization with SARS-CoV-2
640 structural proteins was assessed in ImageJ for (**c**) SARS-CoV-2 S or (**d**) SARS-CoV-2 N. Higher
641 magnification of each overlay image is shown. *$p \leq 0.1$, **$p \leq 0.01$. Representative images are shown
642 from three separate replicate experiments.
643
644 **Fig 3: CNP overexpression inhibits SARS-CoV-2-induced mitochondrial depolarization.**
645 HEK293T/hACE2 cells were infected with SARS-CoV-2/WA1 24-hours following transfection with
646 indicated plasmids. (**a**) 48-hours post-infection, supernatants were collected, and SARS-CoV-2 titers were
647 determined by plaque assay. (**b-c**) At 6-hours post-infection, mitochondrial function was assessed for (**b**)
648 mitochondrial depolarization with JC10 staining or (**c**) opening of the mPTP with TMRM staining. (**d**)
649 HEK293T/hACE2 cells stably overexpressing either CNP or GFP were infected with SARS-CoV-2/WA1
650 (MOI = 5) for 45-minutes followed by washing of any unbound virus. Fresh media containing 10μM
651 Cyclosporin A or DMSO was then immediately added and intracellular SARS-CoV-2 titer determined at
652 18hpi. **$p \leq 0.01$. Representative images are shown for JC10 and TMRM experiments from three
653 replicates.
654
655 **Fig 4: Reactive oxygen species are important for SARS-CoV-2 virion assembly.**
656 (**a**) HEK293T/hACE2 cells were infected with SARS-CoV-2/WA1 24-hours following transfection with
657 indicated plasmids. At 6-hours post-infection, the presence of cytosolic reactive oxygen species was
658 assessed by H_2DCFDA staining. (**b-c**) HEK293T/hACE2 cells stably overexpressing either CNP or GFP
659 were infected with SARS-CoV-2/WA1 (MOI = 5) for 45-minutes followed by washing of any unbound
660 virus. At 3-hours post-infection, cells were treated with a concentration range of hydrogen peroxide. At
661 18-hours post-infection, plaque assays were performed to determine (**b**) intracellular SARS-CoV-2 titers

662 and (**c**) extracellular SARS-CoV-2 titers. *p ≤ 0.1, **p ≤ 0.01, *** p ≤ 0.001, ****p ≤ 0.0001.
663 Representative images are shown for H_2DCFDA staining from three replicates. Virus titer data is the
664 shown for three experiments.
665
666 **Fig 5: CNP transduction reduces SARS-CoV-2 infection in Balb/c laboratory mice.**
667 (**a**) Groups of mice were transduced intranasally with rAd5 vectors (1 x 10^8 viral particles/ mouse) dually
668 expressing hACE2 and either HA-tagged CNP or HA-tagged eGFP 3 days prior to intranasal infection
669 with SARS-CoV-2/WA1 (1 x 10^3 or 1 x 10^5 PFU/mouse). Image created using BioRender. **b-c** Infectious
670 viral loads from lung homogenates were determined by plaque assay at 2- or 4- days post SARS-CoV-2
671 challenge for the (**b**) 1 x 10^3 PFU/mouse or (**c**) 1 x 10^5 PFU/mouse challenge groups. **d-e** Virus titers were
672 also determined by RT-qPCR for sgRNA for the (**d**) 1 x 10^3 PFU/mouse or (**e**) 1 x 10^5 PFU/mouse
673 challenge groups. *** p ≤ 0.001, ****p ≤ 0.0001. Virus titer data is the shown for three experiments.
674
675
676 **S1 Fig: CNP overexpression validation**
677 (**a**) HA-tag staining of HEK293T/hACE2 cells transduced with lentivirus vectors expressing either HA-
678 tagged CNP or HA-tagged eGFP and maintained under selection media. (**b**) Western blots from
679 HEK293T/hACE2 cells transfected with CNP mutation and deletion plasmid constructs stained for HA-
680 tag or Actin controls. (c) Colocalization of HA-tagged CNP constructs in A549/hACE2 cells with
681 mitochondrial staining by mitotracker. Merged images show DAPI, anti-HA and mitotracker
682 colocalization. Image is representative of triplicate samples.
683
684 **S2 Fig: Mitochondrial Function Staining with MOCK infection images**
685 Images correspond to Fig 3. HEK293T/hACE2 cells were infected with SARS-CoV-2/WA1 or MOCK
686 infected 24-hours following transfection with indicated plasmids. At 6-hours post-infection,

687 mitochondrial function was assessed for (**a**) opening of the mPTP with TMRM staining, (**b**) reactive
688 oxygen species staining with H_2DCFDA, or (**c**) mitochondrial depolarization with JC10 staining.
689
690 **S3 Fig: Validation of dual expressing adenovirus vectors in Balb/c laboratory mice.**
691 (**a**) Groups of mice were transduced intranasally with rAd5 vectors (1 x 10^8 viral particles per mouse)
692 dually expressing hACE2 and either HA-tagged CNP or HA-tagged eGFP. Image created using
693 BioRender. (**b**) Weight changes were determined at 3 days post-transduction, plotted as the group mean
694 with error bars indicating the ±SD. **c-d** Lungs were collected at 3-days post-transduction and co-stained
695 by immunofluorescence staining for (**c**) nucleus (blue) and hACE2 (green) or (**d**) nucleus (blue) and HA-
696 tag (purple). **e-f** RT-qPCR was performed for lung homogenates collected at 3-days post-transduction for
697 (**e**) hACE2 and (**f**) CNP. *$p \leq 0.1$, **$p \leq 0.01$.
698
699

700 # Supplemental Table / Figures

701 **S1 Table: RT-qPCR primers.**

Gene Target	Forward (5' to 3') or Company (Cat#)	Reverse (5' to 3') or Company (Cat#)	Detection Method
sgRNA (SARS2 N)	ctcttgtagatctgttctctaaacgaac	ggtccaccaaacgtaatgcg	SYBR Green
gRNA (SARS2 RdRp)	Integrated DNA Technologies (*10006860*)	Integrated DNA Technologies (10006881)	SYBR Green
Human ACE2	------- Integrated DNA Technologies (*Hs01085333_m1*) -------		SYBR Green
Human CNP	----- Integrated DNA Technologies (*Hs.PT.58.27238178*) -----		FAM Probe
Mouse GAPDH	--------- Integrated DNA Technologies (*Mm.PT.39a.1*) ----------		SYBR Green
Human GAPDH	----- Integrated DNA Technologies (*Hs.PT.39a.22214836*) -----		SYBR Green

702 Abbreviations: "sgRNA": subgenomic RNA; "gRNA": genomic RNA; "ACE2": human angiotensin

703 converting enzyme II; "CNP": human 2',3' cyclic-nucleotide 3', phosphodiesterase; "GAPDH":

704 glyceraldehyde-3-phosphate dehydrogenase;

705

706

707 **S2 Table: Infusion cloning primers.**

Gene Target (mutations)	Frag.	Forward (5' to 3')	Reverse (5' to 3')
hCNP	N/A	tcattttggcaaagaattcaccatgaacagaggcttctcc	atcataagggtacatcccgggtatgatggtgcagga
hCNP-CatMut *(H251A, T253A, H330A, T332A)*	1	tcattttggcaaagaattcaccatgaacagaggcttctcc	aacttggtagcgcaagccagcacgcctgg
	2	ttgcgctaccaagttttgtgactacg	cagccgagagcgatagcggcgcggctccc
	3	tatcgctctcggctgtgca	atcataagggtacatcccgggtatgatggtgcagga
hCNP-PrenMut (*C418A*)	N/A	tcattttggcaaagaattcaccatgaacagaggcttctcc	aagggtacatcccgggtatgatggtggcggactgca aggc
hCNPΔMTS (Δ*1-20*)	N/A	ttttggcaaagaattcatgtcatcctcaggggcca	atcataagggtacatcccgggtatgatggtgcagga
hCNPΔPloop (Δ*36-148*)	N/A	agtttcccgagcccaagacggcgtgg	tgggctcgggaaactgcagctcaggc
hCNPΔCat (Δ*185-399*)	N/A	agaaggacaaaggcaaacctgtgccc	tgcctttgtccttctccagcccaggc

708 Abbreviations: "hCNP": human 2',3' cyclic-nucleotide 3', phosphodiesterase; "CatMut": catalytic site

709 mutation; "PrenMut": prenylation site mutation; "MTS", mitochondrial targeting sequence; "Cat":

710 catalytic domain;

711

712

713

714

715 **S3 Table: Antibodies for *in vitro* Western Blot and Immunofluorescent staining**

Assay	Target (Detection)	Antibodies (animal, cat#, supplier)	Staining Conc.
Western Blot	**HA-tag** (HRP)	1°: Rabbit; H6908 (Sigma)	0.6 µg/mL
		2°: Goat α-rabbit HRP; 31460 (Invitrogen)	0.4 µg/mL
	SARS2 S (HRP)	1°: Rabbit; NB100-56578 (Novus)	1.0 µg/mL
		2°: Goat α-rabbit HRP; 31460 (Invitrogen)	0.4 µg/mL
	SARS2 N (HRP)	1°: Rabbit; 40143-R004 (Sino Biologicals)	1.0 µg/mL
		2°: Goat α-rabbit HRP; 31460 (Invitrogen)	0.4 µg/mL
	Actin (HRP)	1°: Mouse; Ab7817 (Abcam)	1.0 µg/mL
		2°: Goat α-mouse HRP; 31430 (Invitrogen)	0.2 µg/mL
IFA (*in vitro*)	**HA-tag** (alexa488)	1°: Chicken; Ab9111 (Abcam)	1.0 µg/mL
		2°: Goat α-chicken 488; A11039 (Invitrogen)	1.0 µg/mL
	HA-tag (alexa647)	1°: Chicken, Ab9111 (Abcam)	1.0 µg/mL
		2°: Goat α-chicken 647; A21449 (Invitrogen)	1.0 µg/mL
	SARS2 S (alexa594)	1°: Rabbit; NB100-56578 (Novus)	1.0 µg/mL
		2°: Donkey α-Rabbit 594; Ab150064 (Abcam)	1.0 µg/mL
	SARS2 N (alexa594)	1°: Rabbit; 40143-R004 (Sino Biologicals)	1.0 µg/mL
		2°: Donkey α-Rabbit 594; Ab150064 (Abcam)	1.0 µg/mL
	ERGIC53 (alexa647)	1°: Mouse; ABS300-100 (Enzo)	10.0 µg/mL
		2°: Goat α-mouse 647; A21235 (Invitrogen)	1.0 µg/mL
IFA (histology)	**hACE2** (alexa488)	1°: Goat; AF933 (R&D)	2.0 µg/mL
		2°: Rabbit α-Goat 488; Ab11078 (Abcam)	2.0 µg/mL
	HA-tag (alexa647)	1°: Chicken, Ab9111 (Abcam)	10.0 µg/mL
		2°: Goat α-chicken 647; A21449 (Invitrogen)	2.0 µg/mL

716 Abbreviations: "Conc.": concentration; "HRP": horse radish peroxidase; "IFA": immunofluorescence

717 assay; "SARS2": SARS-CoV-2; "N": nucleocapsid protein; "S": spike protein; "hACE2": human ACE2;

718

719

720

721

FIGURE 1

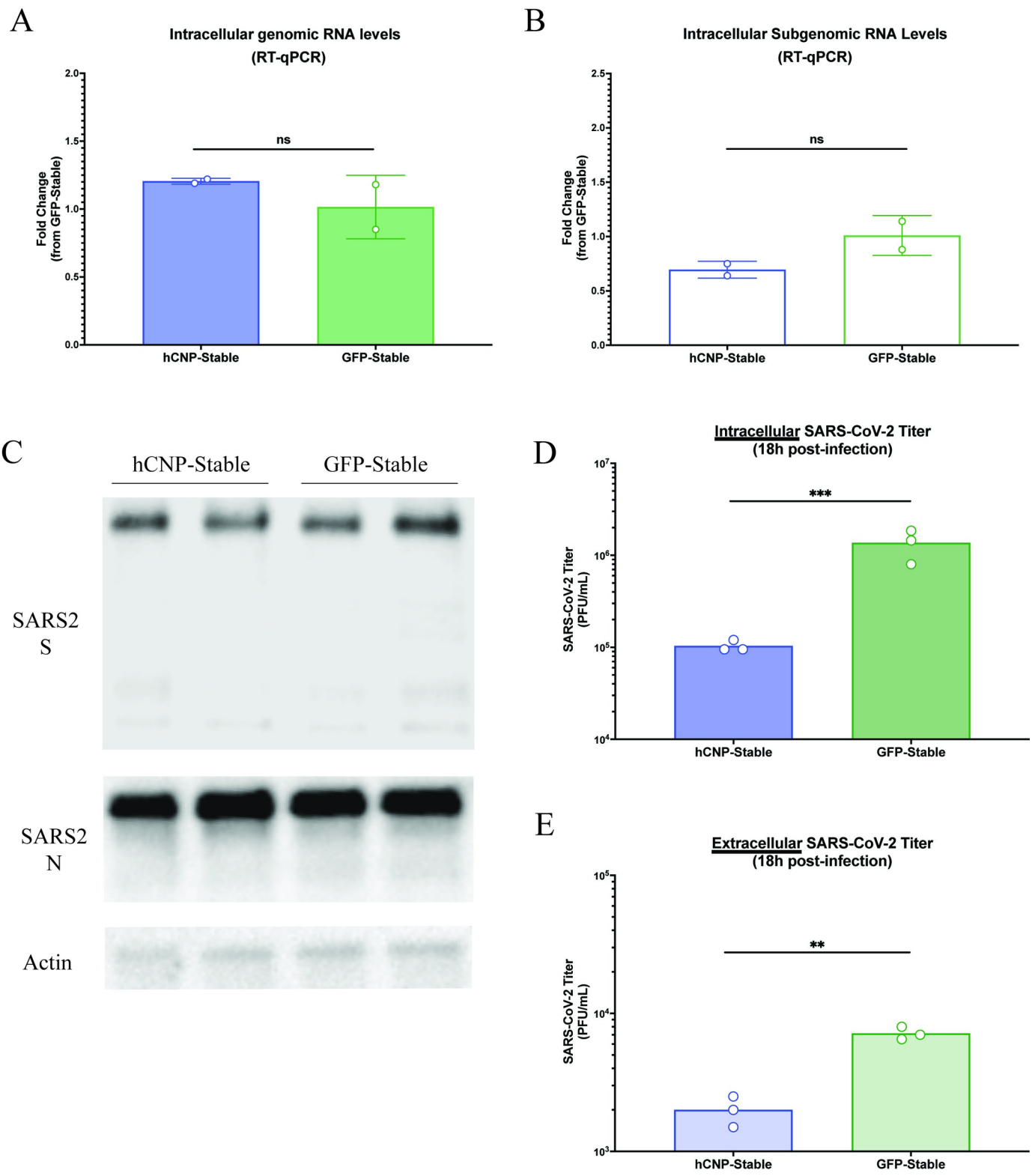
A
Intracellular genomic RNA levels
(RT-qPCR)
Fold Change
(from GFP-Stable)
2.0
1.5
1.0
0.5
0.0
ns
hCNP-Stable
GFP-Stable
B
Intracellular Subgenomic RNA Levels
(RT-qPCR)
Fold Change
(from GFP-Stable)
2.5
2.0
1.5
1.0
0.5
0.0
ns
hCNP-Stable
GFP-Stable
C
hCNP-Stable
GFP-Stable
SARS2
S
SARS2
N
Actin
D
Intracellular SARS-CoV-2 Titer
(18h post-infection)
SARS-CoV-2 Titer
(PFU/mL)
10^7
10^6
10^5
10^4
***
hCNP-Stable
GFP-Stable
E
Extracellular SARS-CoV-2 Titer
(18h post-infection)
SARS-CoV-2 Titer
(PFU/mL)
10^5
10^4
10^3
**
hCNP-Stable
GFP-Stable

FIGURE 2

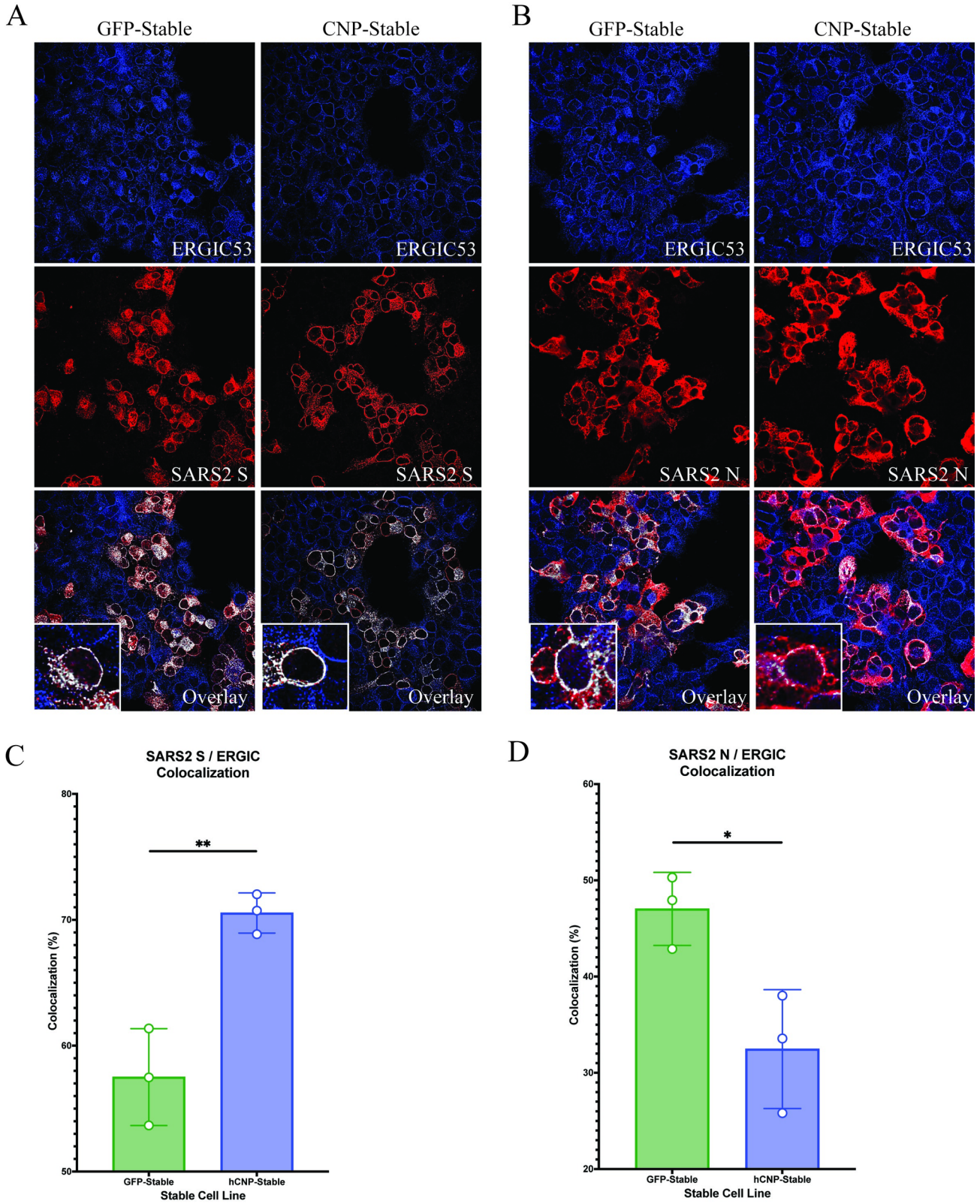
A
GFP-Stable
CNP-Stable
ERGIC53
ERGIC53
SARS2 S
SARS2 S
Overlay
Overlay
B
GFP-Stable
CNP-Stable
ERGIC53
ERGIC53
SARS2 N
SARS2 N
Overlay
Overlay
C
SARS2 S / ERGIC
Colocalization
Colocalization (%)
80
70
60
50
**
GFP-Stable
hCNP-Stable
Stable Cell Line
D
SARS2 N / ERGIC
Colocalization
Colocalization (%)
60
50
40
30
20
*
GFP-Stable
hCNP-Stable
Stable Cell Line

FIGURE 3

A

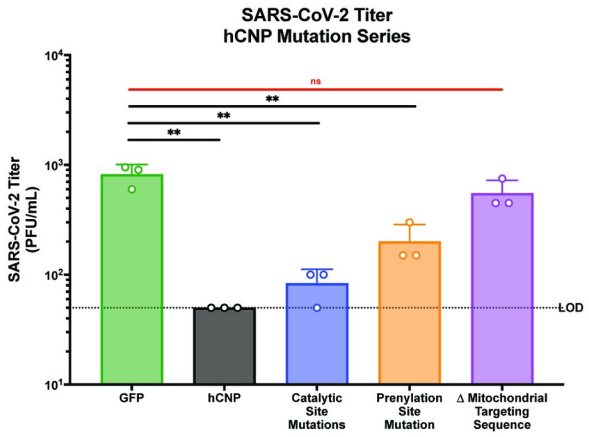

B

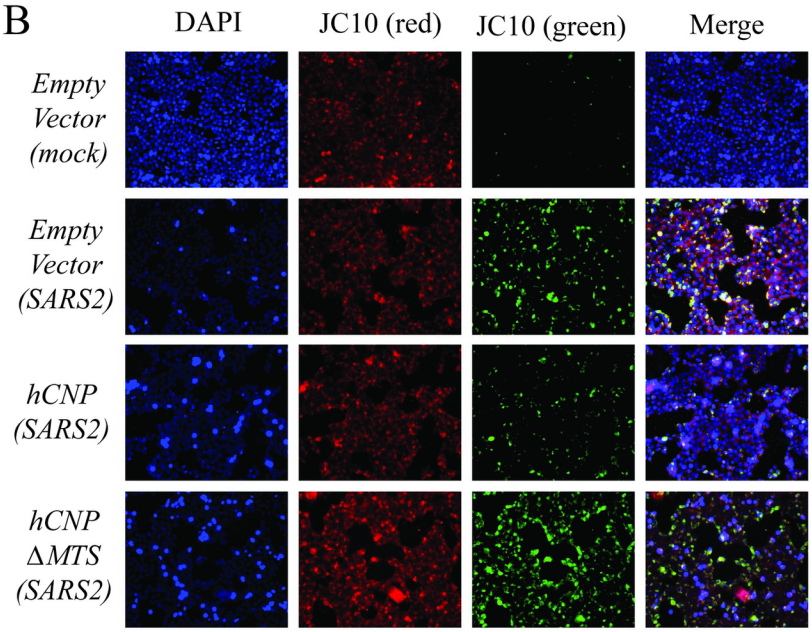

C

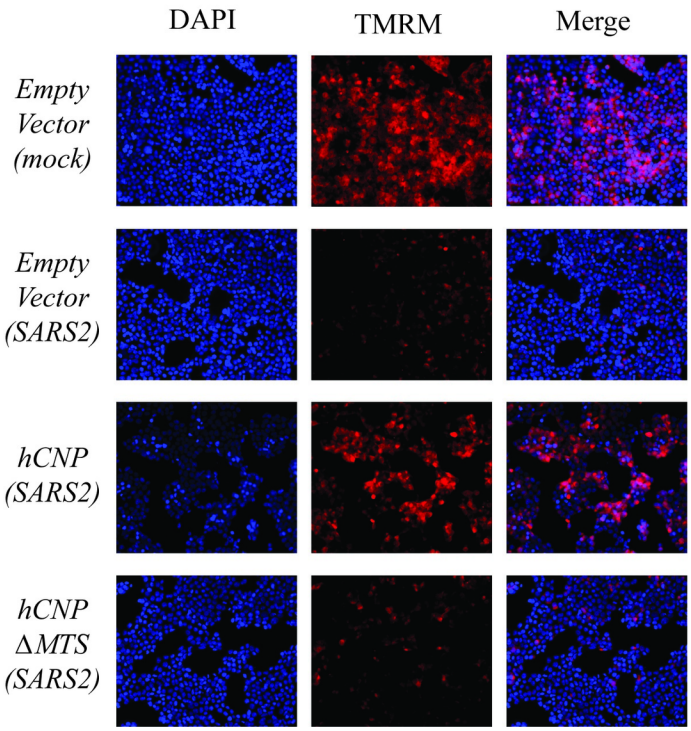

D

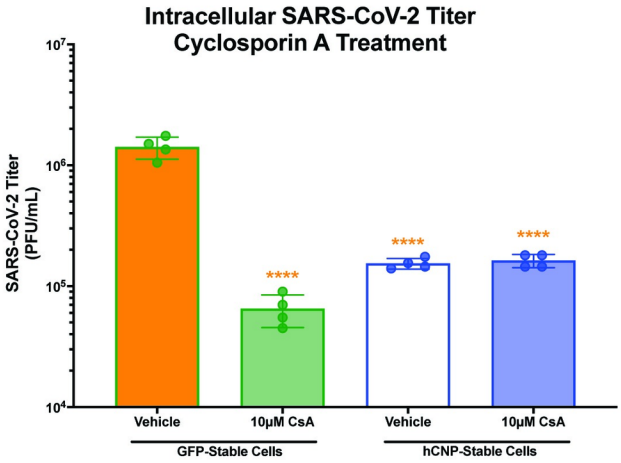

FIGURE 4

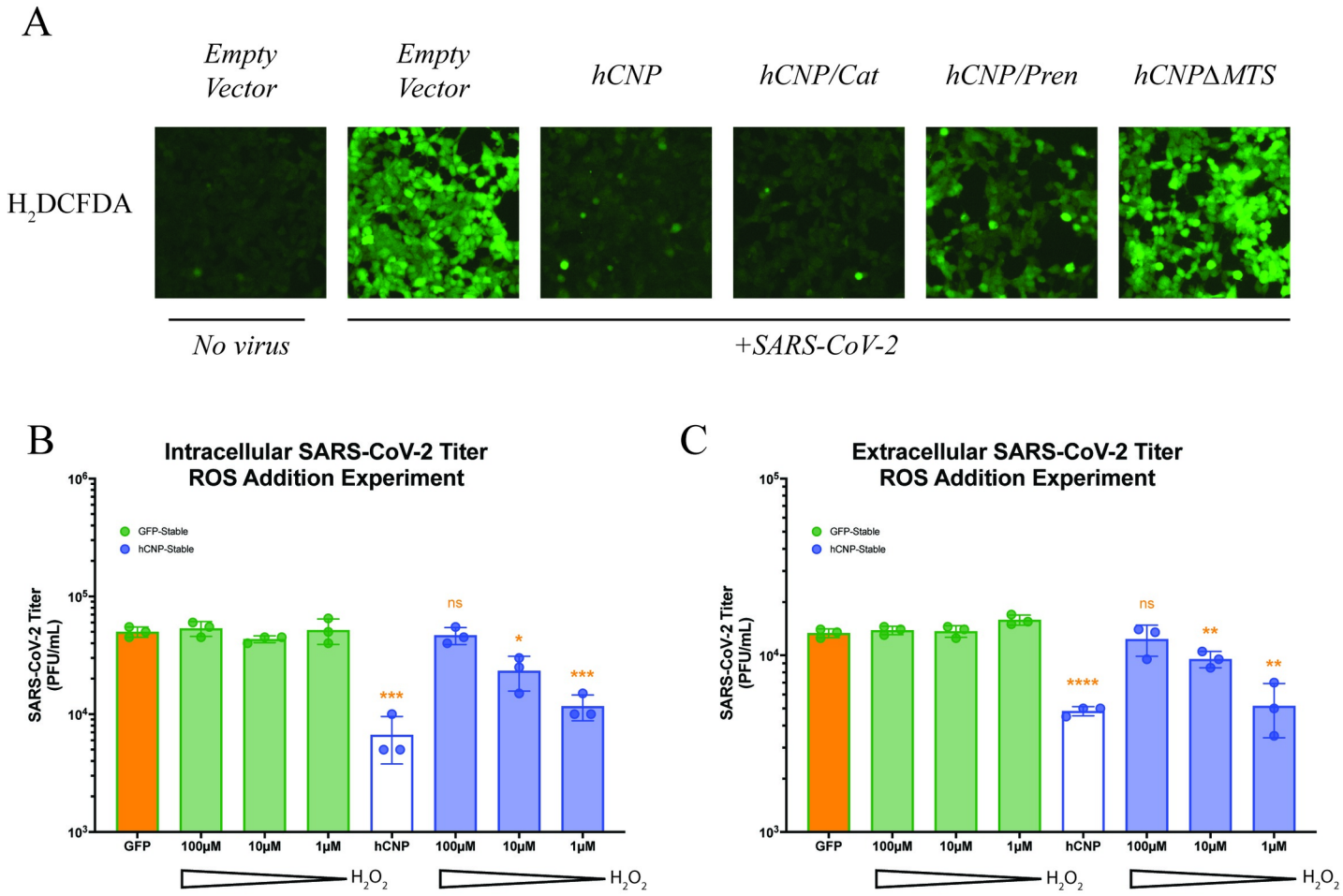
A
Empty Vector
Empty Vector
hCNP
hCNP/Cat
hCNP/Pren
hCNPΔMTS
H2DCFDA
No virus
+SARS-CoV-2
B
Intracellular SARS-CoV-2 Titer
ROS Addition Experiment
GFP-Stable
hCNP-Stable
SARS-CoV-2 Titer (PFU/mL)
GFP
100μM
10μM
1μM
hCNP
100μM
10μM
1μM
H2O2
H2O2
C
Extracellular SARS-CoV-2 Titer
ROS Addition Experiment
GFP-Stable
hCNP-Stable
SARS-CoV-2 Titer (PFU/mL)
GFP
100μM
10μM
1μM
hCNP
100μM
10μM
1μM
H2O2
H2O2

FIGURE 5

A

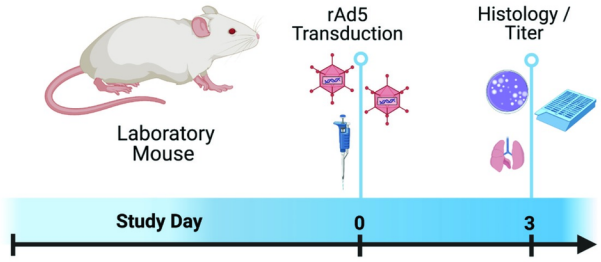

B

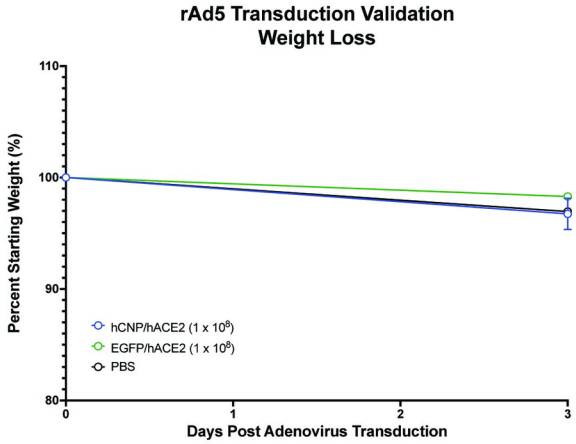

C

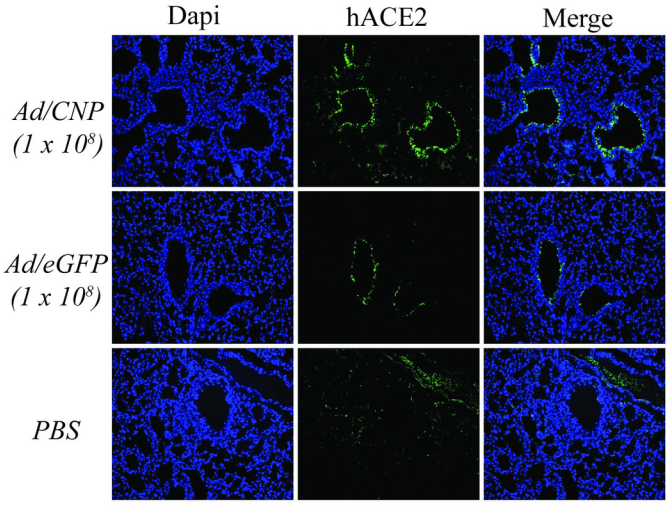

D

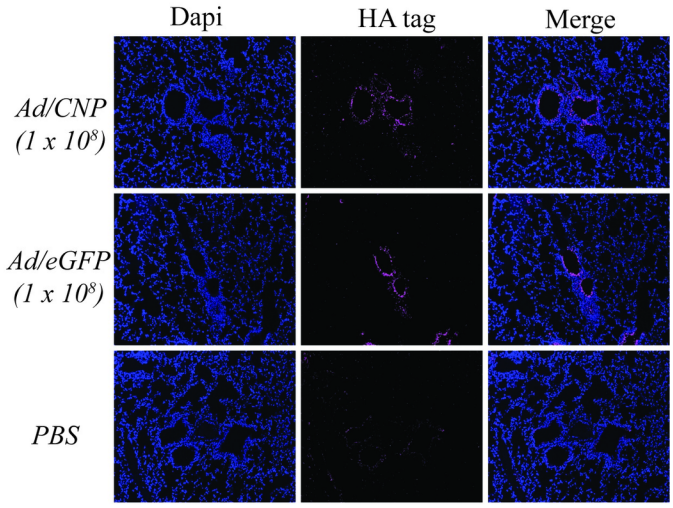

E

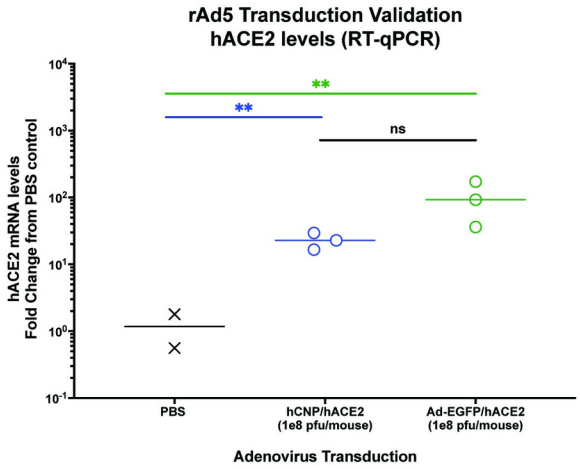

F

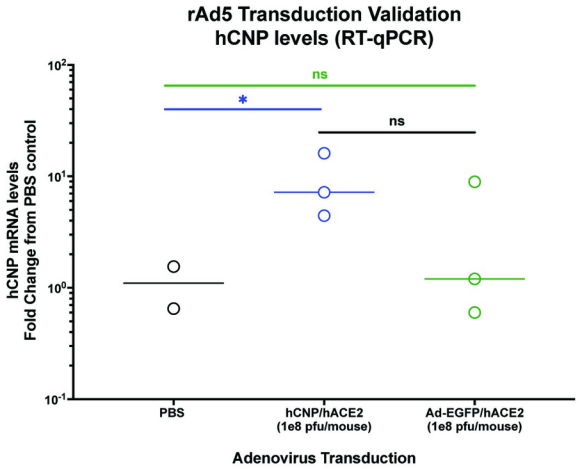

FIGURE 6

A

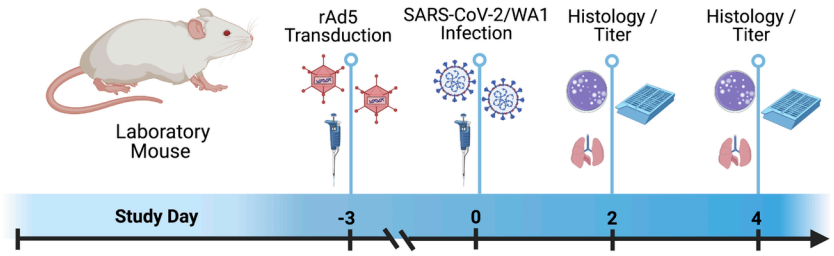

B

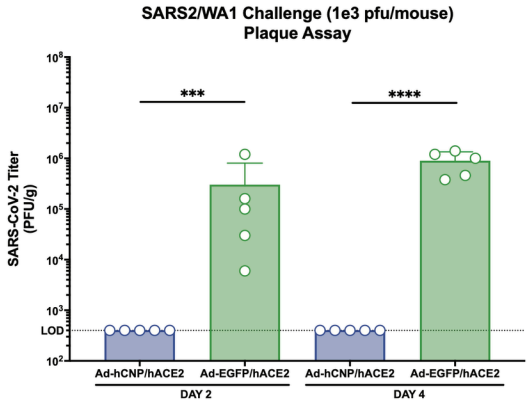

C

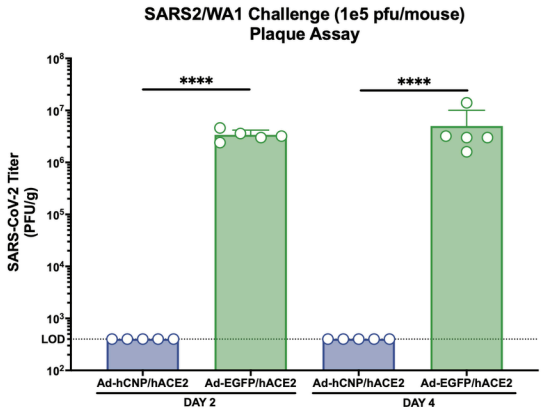

D

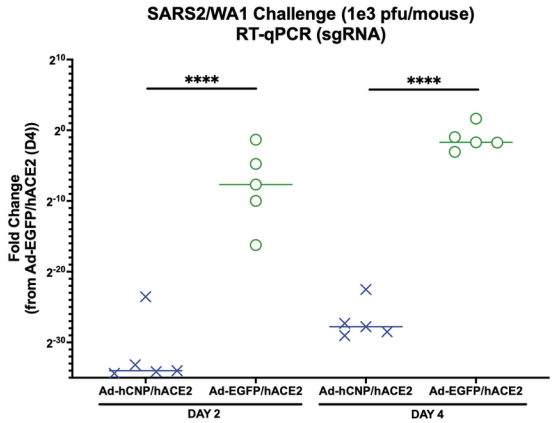

E

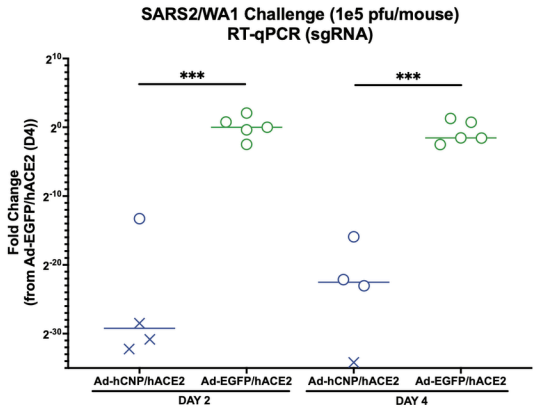

FIGURE S1

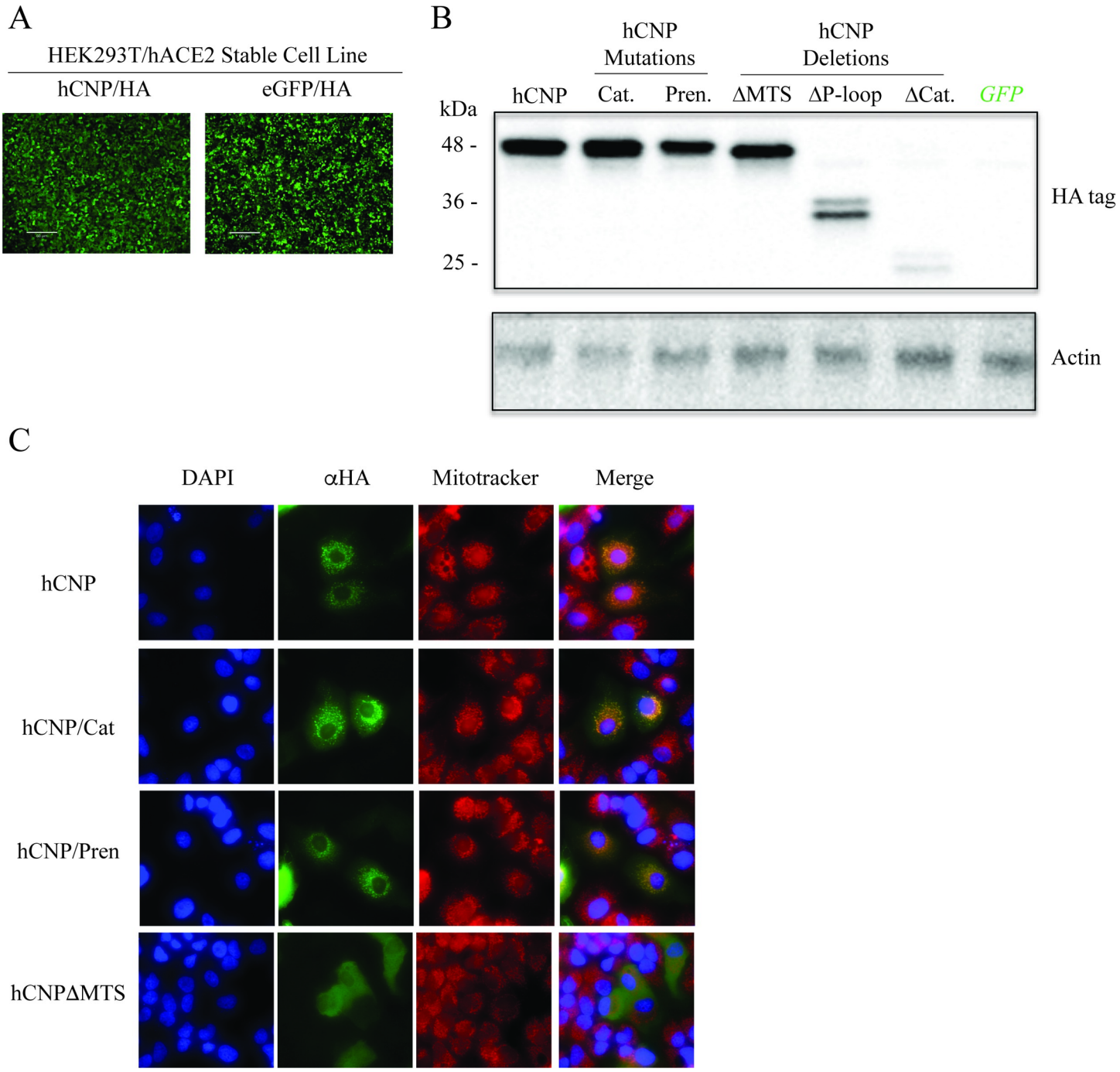
A
HEK293T/hACE2 Stable Cell Line
hCNP/HA
eGFP/HA
B
hCNP Mutations
hCNP Deletions
kDa
hCNP
Cat.
Pren.
ΔMTS
ΔP-loop
ΔCat.
GFP
48 -
36 -
25 -
HA tag
Actin
C
DAPI
αHA
Mitotracker
Merge
hCNP
hCNP/Cat
hCNP/Pren
hCNPΔMTS

FIGURE S2

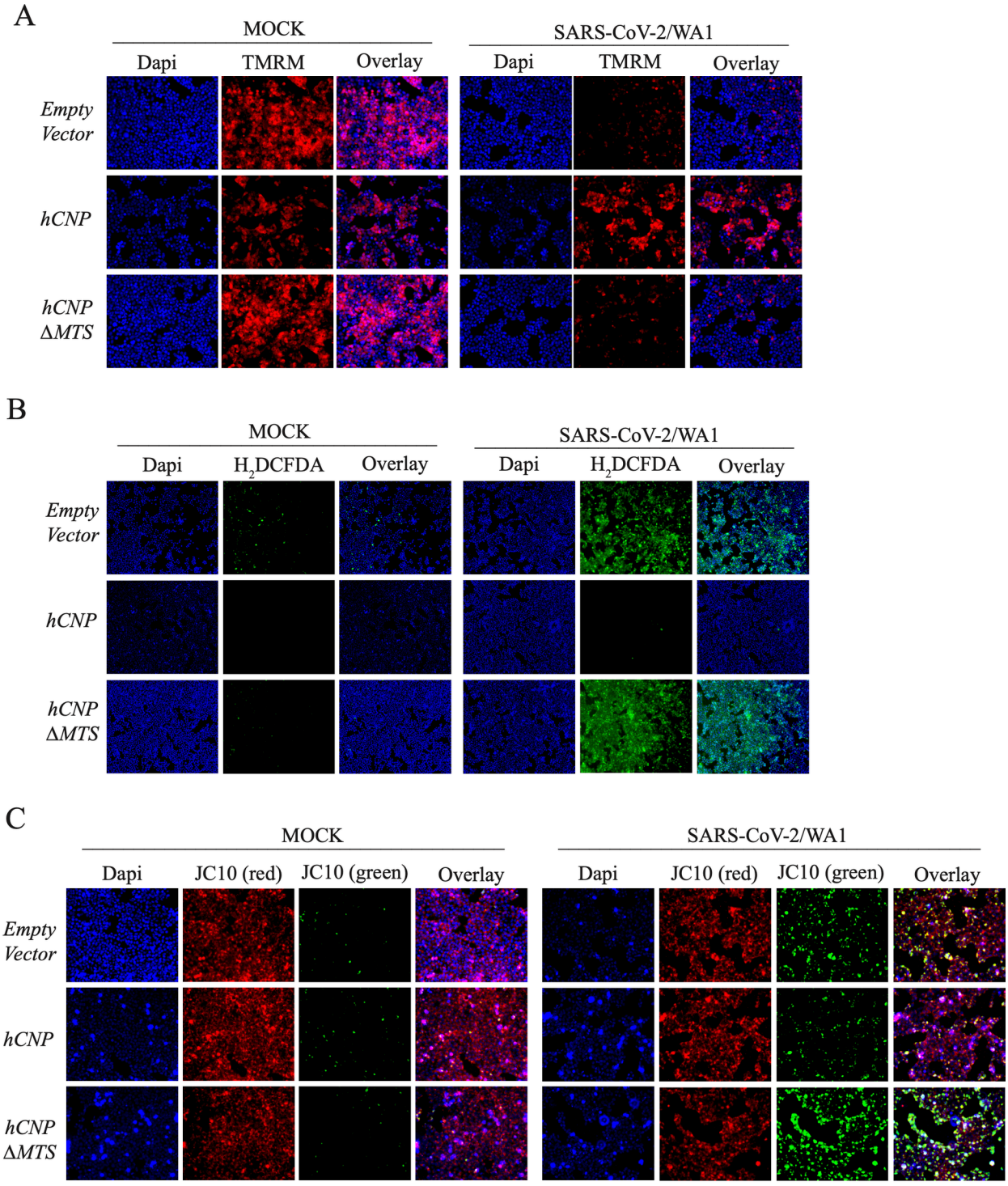
A
MOCK
SARS-CoV-2/WA1
Dapi
TMRM
Overlay
Empty Vector
hCNP
hCNP ΔMTS
B
MOCK
SARS-CoV-2/WA1
Dapi
H2DCFDA
Overlay
Empty Vector
hCNP
hCNP ΔMTS
C
MOCK
SARS-CoV-2/WA1
Dapi
JC10 (red)
JC10 (green)
Overlay
Empty Vector
hCNP
hCNP ΔMTS
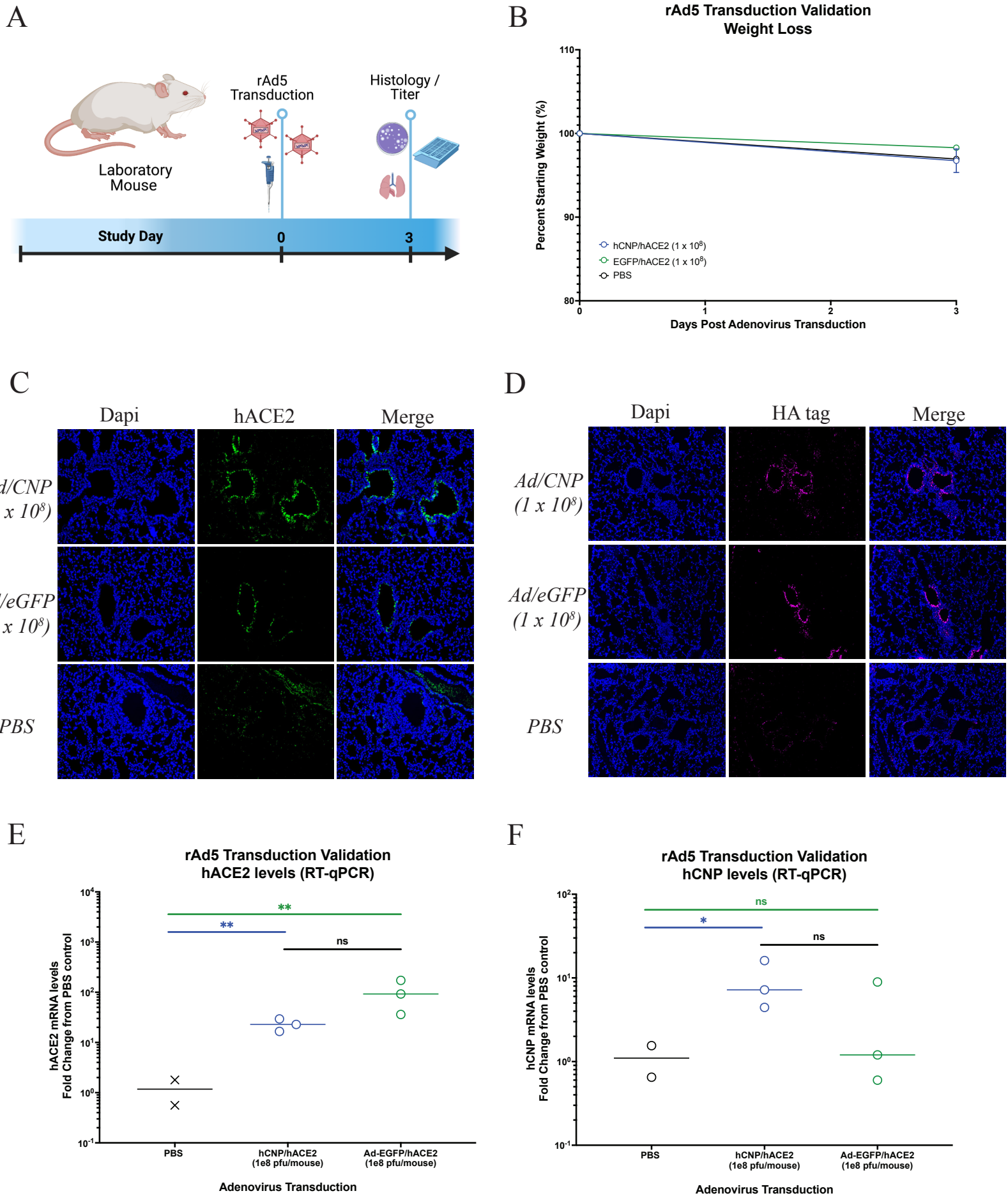
Supplemental Figure 3